

JGR Solid Earth



RESEARCH ARTICLE

10.1029/2022JB025669

High-Resolution InSAR Reveals Localized Pre-Eruptive Deformation Inside the Crater of Agung Volcano, Indonesia

M. J. W. Bemelmans^{1,2} , J. Biggs^{1,2} , M. Poland³ , J. Wookey¹ , S. K. Ebmeier^{2,4} ,
A. K. Diefenbach⁵ , and D. Syahbana⁶ 

¹School of Earth Sciences, University of Bristol, Bristol, UK, ²COMET: Centre for Observation and Modelling of Earthquakes, Volcanoes, and Tectonics, Nottingham, UK, ³U.S. Geological Survey, Cascades Volcano Observatory, Vancouver, WA, USA, ⁴School of the Environment, University of Leeds, Leeds, UK, ⁵U.S. Geological Survey, Volcano Disaster Assistance Program (VDAP), Vancouver, WA, USA, ⁶Center of Volcanology and Geological Hazard Mitigation, Kota Bandung, Indonesia

Key Points:

- We analyze high-resolution Interferometric Synthetic Aperture Radar data from before the November 2017 eruption of Agung, Indonesia, and find localized deformation
- ~15 cm of intra-crater deformation occurred in September-October, with another 3–5 cm in the 4–0.5 days before the first phreatomagmatic explosion
- Magmatic fluids emitted by a flank dyke pressurized the shallow (<200 m) hydrothermal system, causing precursory deformation

Supporting Information:

Supporting Information may be found in the online version of this article.

Correspondence to:

M. J. W. Bemelmans,
mark.bemelmans@bristol.ac.uk

Citation:

Bemelmans, M. J. W., Biggs, J., Poland, M., Wookey, J., Ebmeier, S. K., Diefenbach, A. K., & Syahbana, D. (2023). High-resolution InSAR reveals localized pre-eruptive deformation inside the crater of Agung volcano, Indonesia. *Journal of Geophysical Research: Solid Earth*, 128, e2022JB025669. <https://doi.org/10.1029/2022JB025669>

Received 23 SEP 2022
Accepted 19 APR 2023

Author Contributions:

Conceptualization: J. Biggs, M. Poland
Data curation: M. J. W. Bemelmans, M. Poland, A. K. Diefenbach, D. Syahbana
Formal analysis: M. J. W. Bemelmans, A. K. Diefenbach
Funding acquisition: J. Biggs, M. Poland
Investigation: M. J. W. Bemelmans
Methodology: M. J. W. Bemelmans, J. Biggs, S. K. Ebmeier
Resources: J. Biggs, M. Poland, D. Syahbana

© 2023. The Authors.

This is an open access article under the terms of the [Creative Commons Attribution License](https://creativecommons.org/licenses/by/4.0/), which permits use, distribution and reproduction in any medium, provided the original work is properly cited.

Abstract During a volcanic crisis, high-rate, localized deformation can indicate magma close to the surface, with important implications for eruption forecasting. However, only a few such examples have been reported, because frequent, dense monitoring is needed. High-resolution Synthetic Aperture Radar (SAR) is capable of achieving <1 m spatial resolution and sub-weekly revisit times, but is under-used. Here we use high-resolution satellite SAR imagery from COSMO-SkyMed, TerraSAR-X, and Sentinel-1 to detect intra-crater uplift preceding the November 2017 onset of eruptive activity at Agung, Indonesia. Processing the SAR imagery with an up-to-date, accurate, high-resolution digital elevation model was crucial for preventing aliasing of the deformation signal and for accurate georeferencing. We show that >15 cm of line-of-sight shortening occurred over a 400-by-400 m area on the crater floor in September-October 2017, accompanying a deep seismic swarm and flank dyke intrusion. We attribute the deformation to the pressurization of a shallow (<200 m deep) hydrothermal system by the injection of magmatic gases and fluids. We also observe a second pulse of intra-crater deformation of 3–5 cm within 4 days to 11 hr prior to the first phreatomagmatic eruption, which is consistent with interaction between the hydrothermal system and the ascending magma. This phreatomagmatic eruption created the central pathway used during the final stages of magma ascent. Our observations have important implications for understanding unrest and eruption forecasting, and demonstrate the potential of monitoring with high-resolution SAR.

Plain Language Summary At volcanoes, the ground surface can move due to the activity of magma and associated fluids underground. This deformation is a warning sign that can be useful when forecasting volcanic eruptions, especially when the deformation area is small (less than 1–2 km²), indicating that magma or magmatic fluids are close to the surface (less than 1 km deep). High-resolution satellites such as COSMO-SkyMed can measure ground deformation several times per week with better than 1 m resolution and are thereby able to detect and monitor rapid small-area deformation. We use high-resolution elevation and radar satellite data to detect deformation on the crater floor of Mount Agung, Indonesia, occurring before the November 2017 eruption. We show that the crater floor moved toward the satellites by more than 15 cm in September-October 2017, accompanying an earthquake swarm, caused by magma intruding into the flank of the volcano. In the 4 days leading up to the eruption, we see another 3–5 cm of deformation. A shallow body of magmatic fluids less than 200 m below the crater floor was probably responsible for this ground deformation. Our research shows the potential of monitoring volcanoes with high-resolution radar satellites.

1. Introduction

Localized deformation at volcanoes is caused by shallow processes including magma movement, pressurization of a hydrothermal system, or instability of the edifice, and is often observed shortly before or during an eruption (Cassidy et al., 2019). Thus, observing localized deformation is critical for understanding the final stages of magma ascent and eruption forecasting. However, sufficiently frequent and dense spatial observations are rarely available from ground-based instrument networks. High-resolution Interferometric Synthetic Aperture Radar (InSAR) can achieve <1 m spatial resolution and sub-weekly observations (e.g., COSMO-SkyMed (CSK) (Italiana, 2007), TerraSAR-X (TSX) (Mittermayer et al., 2014), and ICEYE (Ignatenko et al., 2020)), making it an excellent tool for the detection, monitoring, and understanding of localized volcano deformation. For example,

Supervision: J. Biggs, M. Poland, J. Wookey, S. K. Ebmeier

Visualization: M. J. W. Bemelmans

Writing – original draft: M. J. W. Bemelmans

Writing – review & editing: J. Biggs, M. Poland, J. Wookey, S. K. Ebmeier

the Committee on Earth Observing Satellites (CEOS) Volcano Pilot and Volcano Demonstrator projects and the Geohazard Supersites and Natural Laboratories (GSNL) volcano supersites have shown how high-resolution SAR data can effectively aid volcano monitoring and unrest response at several volcanoes in Latin America, Indonesia, the Caribbean, and Iceland (S. Dumont et al., 2018; Pritchard, Biggs, et al., 2018; Pritchard et al., 2021). However, high-resolution SAR data are currently under-used, partly due to the lack of open access, scientific (background) monitoring, and slow data retrieval (Poland & Zebker, 2022; Pritchard & Yun, 2018). Therefore, potentially observable volcano deformation events may not have been recorded or identified.

Localized and transient deformation signals observed with tiltmeters have been attributed to explosive or hydrothermal activity (e.g., Manta & Taisne, 2019; Martini et al., 2010), shear stress along the conduit wall (e.g., Green et al., 2006), and shallow magma storage and transport (e.g., K. R. Anderson et al., 2015), and provide vital information on magmatic pathways. Numerical models indicate that these processes only produce observable displacement close to the eruptive vent (Albino et al., 2011), usually within 1 km. However, costs of installation and maintenance as well as difficult and hazardous terrain make ground-based observations close to eruptive vents rare (Pritchard, Biggs, et al., 2018; Salzer et al., 2014). These signals, lasting seconds to hours, have largely evaded InSAR detection because inflation and deflation happen within the orbit repeat time, which is currently ≥ 1 day(s) (e.g., CSK, ICEYE: 1 day, Sentinel-1: 6 or 12 days, TSX: 11 days, down to 4 days in combination with PAZ (Alonso-González et al., 2021)). Steep slopes and surface changes due to snow and ash deposits limit the use of InSAR near eruptive vents because of a loss in coherence (Pinel et al., 2014; Wang et al., 2019). Additionally, the localized nature of these deformation events makes detection with routinely processed open-access satellite InSAR (e.g., Sentinel-1) at ≥ 30 m resolution difficult, requiring tailored higher resolution processing. We have thus potentially been missing both highly localized and transient deformation signals, with exceptions at a few volcanoes with dense ground-based networks (e.g., Kilauea (K. R. Anderson et al., 2015), Etna (Bonforte & Puglisi, 2006), Sakurajima (Hotta, Iguchi, & Ohkura, 2016; Hotta, Iguchi, & Tameguri, 2016), and Soufrière Hills (Jackson et al., 1998; Odbert et al., 2014; Voight et al., 1998)), proof-of-concept satellite studies (e.g., Mania et al., 2019; Richter et al., 2018; Salzer et al., 2014), or serendipitous discoveries (e.g., Richter et al., 2013).

In this study, we use high-resolution InSAR, supplied by the CEOS Volcano Demonstrator Project, to investigate intra-crater deformation preceding the 2017 eruption of Agung volcano, Indonesia, to learn more about the pathways and timing of magmatic and hydrothermal fluid ascent. We use multi-temporal InSAR (MTI) and elastic half-space modeling to assess the time evolution of the deformation as well as estimate the parameters describing its source. Finally, we discuss the implications of high-resolution SAR for volcano monitoring.

2. Background

2.1. Characteristics and Mechanisms of Localized Volcano Deformation

Surface displacement at volcanoes varies widely in duration and deformation area, from minute/hour long syn-eruptive subsidence at Stromboli, Italy (Di Traglia et al., 2021), to centuries long cooling of lava flows (e.g., Kone, Ethiopia (Albino & Biggs, 2021), and Timanfaya, Lanzarote (Purcell et al., 2022)) and from 150 m wide deformation caused by crater wall collapse at Kilauea, Hawaii (Richter et al., 2013), to a 70 km diameter uplift area within an 150 km diameter subsidence area at Uturuncu, Bolivia (Pritchard, de Silva et al., 2018). In general, deformation rates are inversely correlated with deformation area and event duration (Biggs & Pritchard, 2017; Ebmeier et al., 2018). Measurement sensitivity decreases with the depth of the deformation source, making deep and small-magnitude deformation sources more difficult to observe (Ebmeier et al., 2018). InSAR-observed volcano deformation events have an estimated signal area (“footprint”) spanning several orders of magnitude, from ≤ 1 to $\geq 10,000$ km² (Ebmeier et al., 2018). Small-footprint (≤ 10 km²) deformation signals are often attributed to shallow (< 2 km depth) sources, and we expect deformation caused by very shallow sources to be under-represented in these catalogs due to the low spatial resolution of most measurements (Ebmeier et al., 2018). Furthermore, high deformation rates can cause phase incoherence (e.g., co-eruptive displacement at Sierra Nerga, Galapagos, and Ambrym, Vanuatu; Casu et al., 2011; Shreve et al., 2019; Yun et al., 2007), eruption products can cause incoherence in co-eruptive interferograms (e.g., tephra from the 2013 eruption of Volcán de Colima, Mexico; Salzer et al., 2014), and steep slopes and vegetation can cause low signal-to-noise ratio (Pinel et al., 2011), masking possible deformation signals.

High-resolution SAR satellites have identified localized deformation at several volcanoes and are often the only tool available for such observations. Building on the work of Ebmeier et al. (2018), we have compiled 81

SAR-observed volcano deformation events that have a lateral extent ≤ 1 km and/or estimated source depth of ≤ 1 km, representing $\sim 20\%$ of the >450 cataloged volcano deformation events (Table 1). Notably, 32 events are related to dyke intrusions and slope instability at Piton de la Fournaise (Q. Dumont et al., 2022). From those 81 events, 73 were attributed to a physical mechanism, such as: shallow magma transport and storage (including intrusions), conduit processes, hydrothermal system pressurization, cryptodome/laccolith growth or contraction, degassing, and slope instability (Figure 1 and Table 1). In some cases, it is not clear which mechanism is responsible for the deformation, for example, fault-bounded subsidence at Gada Ale (Ethiopia) from 1993 to 1996 was attributed to shallow magma withdrawal (Amelung et al., 2000), whereas similar subsidence from 2015 to 2020 has been attributed to hydrothermal fluids (Albino & Biggs, 2021). We exclude deformation due to cooling deposits because these do not relate to subsurface processes.

Although there are relatively few examples of volcano deformation with subsurface sources shallower than 1 km, many instances of deformation sources at depths between 1 and 3 km have been documented, in particular at active basaltic systems (e.g., Kilauea (Bemelmans et al., 2021; Poland et al., 2014), Sierra Negra (Yun et al., 2006), Mount Okmok (Lu & Dzurisin, 2014), and Piton de la Fournaise (Q. Dumont et al., 2022)). These occurrences are often attributed to magma transport and storage, whereas the mechanisms of shallower (<1 km depth) deformation are frequently cited as a result of hydrothermal activity (see Table 1 and Lu & Dzurisin, 2014; Kobayashi et al., 2018). Shallow hydrothermal systems are often linked to magmatic systems and, even though magma transport and storage at depth might not produce noticeable ground motion, magmatic activity can trigger changes in shallow hydrothermal activity, which can cause surface deformation. Ground displacements from these secondary, shallow processes can therefore be used to indicate, track, and investigate magmatic processes at depth—for example, hydrothermal activity driven by deep magmatic fluid pressurization at Hakone and Midagahara, Japan (Kobayashi, 2018; Kobayashi et al., 2018).

Most of the listed mechanisms can precede eruptions and are therefore important when considering the potential outcome of developing unrest. Shallow sources might give little warning before an eruption. For instance, deformation at the summit of Volcàn de Colima occurred within just 11 days of the 2013 eruption and has been linked to pressurization of sources high within the conduit (Salzer et al., 2014). The small footprint of the deformation signal can also help forecast the eventual eruption site. For example, small-footprint deformation at Hakone and Iwo-Yama (both Japan), related to their shallow hydrothermal systems, corresponded to the sites of the eventual phreatic eruptions (Kobayashi et al., 2018; Narita et al., 2020). Table 1 shows that small-footprint (≤ 1 km length) signals are most frequently observed with high-resolution SAR products from ALOS (2), CSK, TSX, RADARSAT-2 (RS2), UAVSAR and Pi-SAR L2, demonstrating the need for high-resolution SAR products, especially where ground monitoring instruments are sparse or not available. Understanding these shallow processes and their link to deeper magmatic processes helps improve eruption and unrest forecasting at volcanoes like Agung where observations of deep-seated unrest need to be assimilated with those of shallow unrest.

2.2. Geologic Setting and Historical Eruptions of Agung

Agung volcano is a stratovolcano located on the island of Bali in Indonesia. Analysis of eruption frequency from the late Holocene tephrostratigraphic record reveals that Agung experienced 53 tephra producing eruptions in the last 5.2 ky (Fontijn et al., 2015). The last major eruption of Agung took place in 1963 (Kusumadinata, 1964; Self & Rampino, 2012; Zen & Hadikusumo, 1964) and was one of the largest eruptions of the twentieth century, ranking Volcano Explosivity Index (VEI) 5 and causing over 1100 fatalities (Auker et al., 2013; Tanguy et al., 1998). An additional 200 people were killed by lahars that were triggered by intense rainfall after the eruption (Zen & Hadikusumo, 1964, who reported nearly 2000 fatalities in total). Before the 1963 eruption, no monitoring equipment was present on Bali, which was only intermittently visited by the Volcanological Survey of Indonesia to observe Mount Batur because of its 1926 eruption (Zen & Hadikusumo, 1964). A few months after the start of the 1963 eruption at Agung, basalt/basaltic-andesite lavas started erupting from Batur caldera (Kusumadinata, 1964), and Batur remained active into the 1970s. Using thermobarometry of Agung's 1963 eruption products, two magma storage depths can be identified: one deep source around the Mohorovičić discontinuity at 10–30 km depth, and another at the lithological boundary between oceanic crust and sediments at 3–7 km depth (Geiger et al., 2018). Mixing of mafic magma intruding from depth into shallow, more differentiated magma has been proposed as a triggering mechanism for the 1963 (Fontijn et al., 2015; Self & King, 1996) and 2017 (Albino et al., 2019) eruption of Agung.

Table 1

Synthetic Aperture Radar (SAR) Observed Shallow (Depth ≤ 1 km) and/or Localized (Signal Length ≤ 1 km) Volcano Deformation Attributed to the Deformation Mechanisms Shown in Figure 1

Mechanism	Volcano	Length [km]	Depth [km]	SAR platform ^a	Reference
Magma	Alu-Dalafilla	2	1	ALOS, Envisat	Pagli et al. (2012)
Magma	Tungurahua	3–5	≤ 1	TSX	Muller et al. (2018)
				TSX	Hickey et al. (2020)
Magma	A. Krakatau	0.9	0.6	ALOS	Agustan et al. (2012)
Magma	Fernandina	6	0.93	Envisat	Chadwick et al. (2011)
Magma	P d/l F	<1–8	<1	ALOS-2, Envisat, RS1/2, S1, TSX	Q. Dumont et al. (2022) ^b
Magma	Sakurajima	1	0.8	ALOS-2	Morishita et al. (2016)
Conduit	Colima	1	0.2	TSX	Salzer et al. (2014)
Conduit	Láscar	0.5	0.18	ERS	Pavez et al. (2006)
Conduit	Masaya	0.7	0.7	CSK	Stephens et al. (2017)
Conduit	SHV	0.5	1	ERS	Wadge et al. (2006)
Hydro. sys.	Agung	0.4	≤ 0.2	CSK, TSX, S1	This study
Hydro. sys.	Asama	2	1	S1, ALOS-2	Wang et al. (2019)
Hydro. sys.	Gada Ale	3	0.7	ERS	Amelung et al. (2000)
				S1	Albino and Biggs (2021)
Hydro. sys.	Hakone	0.3	0.15	ALOS, RS2, S1	Kobayashi et al. (2018)
Hydro. sys.	Kirishima	0.4–1	0.15–0.7	ALOS-2, Pi-SAR L2	Yunjun et al. (2021)
				ALOS(–2)	Narita et al. (2020)
Hydro. sys.	Kiska	2	0.9	Envisat, ERS	Lu and Dzurisin (2014)
Hydro. sys.	Lastarria	1.5	0.75	Envisat, ERS	Ruch et al. (2009)
Hydro. sys.	Menengai	6	0.7	ERS	Biggs et al. (2009) ^c
Hydro. sys.	Midagahara	0.4	0.05	ALOS	Kobayashi (2018)
Hydro. sys.	Miyage-Jima	3	~ 0.6	ALOS	Ozawa and Ueda (2011)
Hydro. sys.	Sinabung	<1	0.5	ALOS	González et al. (2015)
Hydro. sys.	Tongariro	1.5	0.5	CSK	Hamling et al. (2016)
Cryptodome	Cordón-Caulle	4	≤ 0.2	TSX	Castro et al. (2016)
				TSX, TDX	Delgado et al. (2019)
Cryptodome	Usu	≤ 2	0.2	JERS, RS1	Tobita et al. (2001)
				JERS, ALOS(–2)	Wang and Aoki (2019)
Degassing	Láscar	≤ 0.3	~ 0	TSX	Richter et al. (2018)
Slope inst.	Arenal	4	≤ 0.01	TSX	Ebmeier et al. (2014)
Slope inst.	Kīlauea	0.15	0	TSX	Richter et al. (2013)
Slope inst.	A. Krakatau	1	≤ 0.25	S1	Walter et al. (2019)
Slope inst.	Lastarria	1–2	<1	Envisat, ERS	Ruch et al. (2009)
Slope inst.	Pacaya	3	≤ 0.5	ALOS, UAVSAR	Schaefer et al. (2017); Schaefer et al. (2019)
Slope inst.	P d/l F	<1–8	≤ 1	ALOS-2, Envisat, RS1/2, S1, TSX	Q. Dumont et al. (2022) ^b

Note. Lateral extent and depth are reported from the given literature or estimated from figures therein. When necessary, depth is standardized to km below surface. A. Krakatau is Anak Krakatau, P d/l F is Piton de la Fournaise, SHV is Soufrière Hills Volcano.

^aALOS (or ALOS-2) = Advanced Land-Observing Satellite PALSAR 1 (or 2), ERS = European Remote-Sensing satellite, JERS = Japanese Earth Resources Satellite, S1 = Sentinel-1, RS1 or RS2 = RADARSAT 1 or 2, TDX = TanDEM-X, UAVSAR and Pi-SAR L2 are uncrewed aerial vehicle SAR drones. ^bReferences therein. ^cRevised to movement of fluids (Biggs, internal comms).

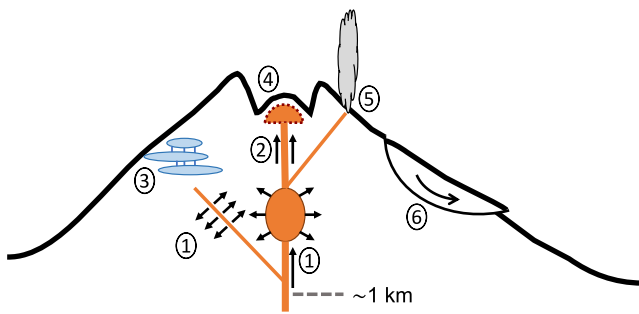


Figure 1. Cartoon cross-section of a volcano showing several physical mechanisms, situated within 1 km depth of the surface, that cause localized surface deformation. 1: Shallow magma transport and storage (including intrusions), 2: Conduit processes, 3: Hydrothermal system (de)pressurization, 4: Cryptodome/Laccolith growth/contraction, 5: Degassing, 6: Slope instability. See Table 1 for examples of where these mechanisms have been observed.

From 1964 to 2017, the volcano was quiet with few local earthquakes recorded (Syahbana et al., 2019). Satellite InSAR seemingly showed inflation centered on the volcano in 2007–2009 (Chaussard & Amelung, 2012), which motivated the installation of a seismic and geodetic network at Agung (Syahbana et al., 2019). However, re-evaluation of the data used in Chaussard and Amelung (2012) showed that the signal at Agung was primarily caused by atmospheric effects with no evidence of inflation at the volcano (Yip et al., 2019). Today, roughly 200,000 people live within the hazard zone, 9–12 km from the volcano summit (Syahbana et al., 2019).

2.3. September–October 2017 Unrest Episode

2.3.1. (Near) Real-Time Observations

Two distinct changes in activity were observed around mid-September 2017 (see Figure 2), which caused the Center for Volcanology and Geological Hazard Mitigation (CVGHM) to increase the alert level at Agung, in stages, from Normal (1/4) before 14 September 2017, to Awas (4/4) on 22 September 2017 (Figure 2 top). First, there was an exponential increase in

seismic activity that began in mid-September and quickly reached >500 events per day, remaining elevated for 4 weeks. The seismic monitoring network was limited to the sparsely distributed national network operated by the Meteorological, Climatological, and Geophysical agency of Indonesia (BMKG), and the CVGHM local

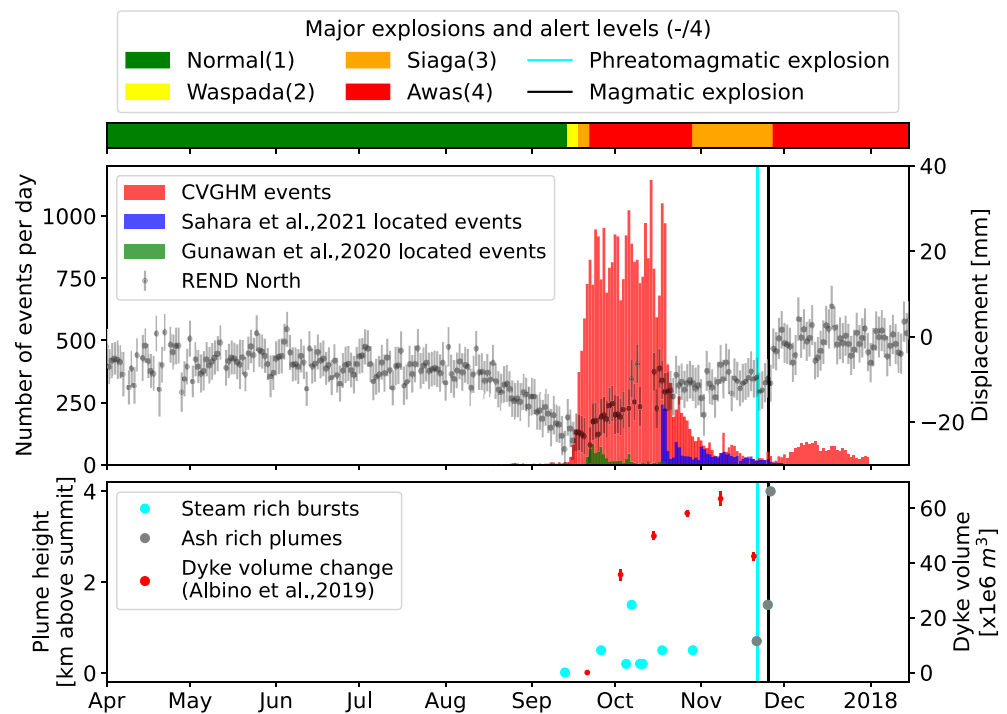


Figure 2. Time series of observations from April 2017 to January 2018. (Top) Alert levels (–/4) by color. (Middle) Seismic activity as daily event count (red) and histogram of hypocenter count per day from Gunawan et al. (2020) (green) who use the Meteorological, Climatological, and Geophysical agency of Indonesia (BMKG) network and Sahara et al. (2021) (blue) who used the local Center for Volcanology and Geological Hazard Mitigation (CVGHM) network (see Figure 3a) completed on 18 October 2017, and show migration of hypocenters toward the summit of Agung from October to November 2017. Gray points and 1σ error bars show North component displacement and uncertainty of the REND Global Positioning System (GPS) station located 12 km southwest from Agung (see Figure 3a). Bottom) Height of steam (cyan dots)- and ash (gray dots)-rich plumes above the summit of Agung. The phreatomagmatic explosion on 21 November 2017, was the first ash-rich plume. Red dots and error bars show estimated dyke volume through time from Albino et al. (2019). Vertical cyan and black lines indicate the time of the first phreatomagmatic and magmatic explosions, respectively.

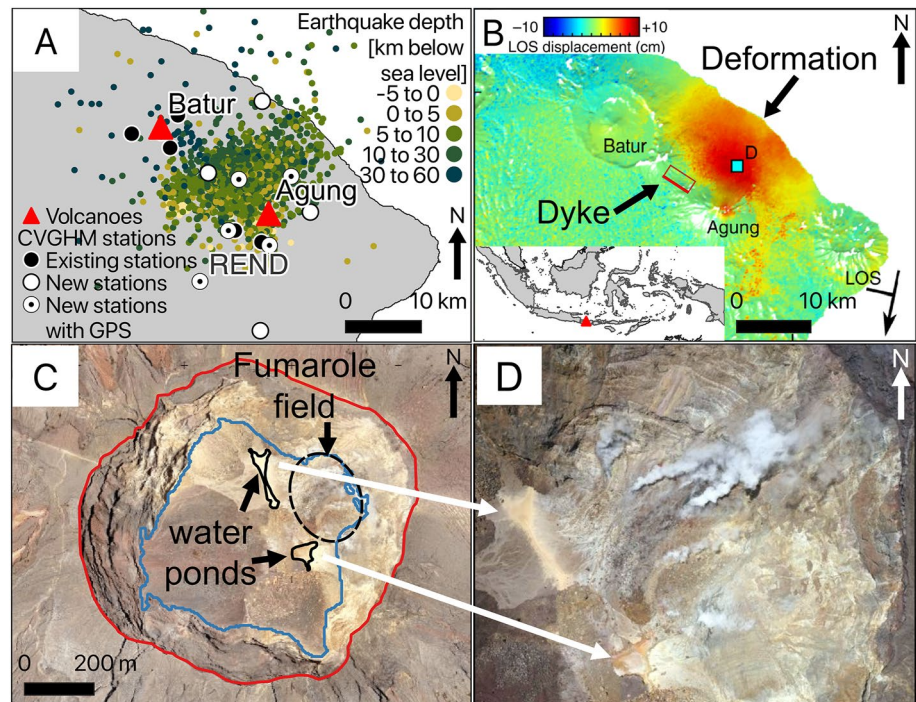


Figure 3. Regional setting of Agung with ground measurement stations and earthquake hypocenters. (a) Map of Agung and Batur with local measurement stations; black circles show existing stations, which collected data during the September-October unrest, white circles are stations that were newly installed or revived following the unrest, white circles with black dot are new stations with GPS. Station REND, used in Figure 2, is labeled for reference. Earthquake hypocenters from Gunawan et al. (2020) and Sahara et al. (2021) are shown with depth below mean sea level. Volcanoes are shown as red triangles. (b) Sentinel-1 descending displacement from August to November 2017, adapted from (Albino et al., 2019). Modeled dyke outline shown in red. Cyan square labeled “D” is used for time series analysis in Albino et al. (2019). The inset in B shows the location of Agung (red triangle) on a map of Indonesia. (c) Orthographic image of the summit of Agung taken by UAV on 20 October 2017, image credit: CVGHM. Crater rim and crater floor shown in red and blue, respectively, and are shown in all subsequent figures showing the summit crater. The outline of two water ponds (Andaru et al., 2021) is shown in black, and the dashed ellipse shows the location of the fumarole field. The white arrows point from the water ponds in Panel C to the same ponds in panel (d) (d) UAV image of the northeastern part of the crater showing the water ponds and the fumarole field. Image taken on 20 October 2017, image credit: CVGHM.

network consisting of three stations at Batur and two stations at Agung (see Figure 3a). Near-real-time hypocenter locations with a resolution of ~ 1 km were available from the BMKG network and showed that seismicity in September-October was primarily located between Agung and Batur (Albino et al., 2019; Syahbana et al., 2019). Second, increased fumarolic activity and several steam-rich bursts, originating from the summit, were observed in September-October 2017 (see Figures 2 and 3d) (Albino et al., 2019; Syahbana et al., 2019). This was a sign that a hydrothermal system at the summit was involved in the activity from the start of volcanic unrest. A particularly strong steam burst with a plume height of 1.5 km occurred on 9 October 2017. Thermal observations showed a small increase in radiance from the crater at the start of the unrest in September; however, the radiance dropped below the pre-unrest maximum in October (Syahbana et al., 2019). The heightened seismic activity and displacement lasted approximately 4 weeks before diminishing in mid-October (see Figure 2). Seismicity continued from October to November, but at a slower rate, introducing large forecasting uncertainties (Syahbana et al., 2019; Wellik et al., 2021). Eventually, CVGHM lowered the alert level to Siaga (3/4) on 29 October 2017. None of the 12 mobile Differential Optical Absorption Spectrometry (DOAS) campaigns performed from 1 October to 14 November 2017, were able to detect SO_2 emissions (Syahbana et al., 2019).

2.3.2. Retrospective Analysis

Retrospective analysis revealed the mechanism responsible for the changes in activity observed in 2017. Sentinel-1 InSAR data from September-October showed ~ 6 cm of displacement toward the satellite north of Agung (Albino et al., 2019; Syahbana et al., 2019). Displacement continued at a slower rate resulting in a total

of ~10 cm by November 2017 (see Figure 3b) (Albino et al., 2019, 2020). The InSAR-observed displacements were attributed to a flank dyke intrusion between Agung and the neighboring volcano Batur (Figure 3b) (Albino et al., 2019, 2020). This dyke intruded at a depth of 7–13 km and is oriented NW-SE following the local stress field controlled by topographic loading of Agung and Batur (Albino et al., 2019). Albino et al. (2019) also discussed a possible shallow deformation source, coincident with the flank dyke intrusion, at the summit estimated at 1 km below the surface; however, this source could be atmospheric in nature as atmospheric corrections were not able to account for short-wavelength (<10 km) atmospheric perturbations that were expected to be present at high (>2 km) elevation (Albino et al., 2020).

GPS data were recorded at 5 locations around Agung since 2012. However, transmission issues prevented (near) real-time analysis at all sites since 2014 until the network was revived in late 2017, after the majority of seismic unrest (see Figure 2) (Syahbana et al., 2019). The GPS data revealed displacement away from the volcano, indicative of deep-seated (10–20 km depth) inflation, in February-March and August-September of 2017 (Syahbana et al., 2019). GPS displacements changed direction in mid-September 2017 (see Figure 2), and were attributed to the dyke intrusion as well as deep-seated deflation (Syahbana et al., 2019).

Detailed post-eruption analysis of the precursory seismic data (including improving the hypocenter locations, see Figure 3a) confirmed that, even though activity had dropped, the location of the seismic events progressed toward the summit of Agung from October to November 2017 (Sahara et al., 2021; Syahbana et al., 2019). Additionally, grouping the seismic signals into self-similar families showed a transition in the characteristics of seismic events from intrusive to eruptive around November 12–15, 2017 (Wellik et al., 2021).

2.4. November 2017 Eruption

The eruption started 09:05 (UTC) on 21 November 2017, and created a 100-m-diameter explosion crater located in the middle of the crater floor (Syahbana et al., 2019). Several explosive events followed and lava flows were first detected on the crater floor on 25 November 2017 (Syahbana et al., 2019). On 27 November 2017, a dark ash-rich and white steam-rich plume emerged simultaneously from the summit, after which the entire crater floor was inundated with lava (Syahbana et al., 2019). By 16 December 2017, an estimated $26.86 \pm 0.64 \times 10^6$ m³ of lava had filled the summit crater with a maximum thickness of 126 m (Andaru et al., 2021). Notably, during 8–20 November, 2017, the volume of the flank dyke dropped by approximately 21×10^6 m³ (Albino et al., 2019). These volume estimates suggest that a similar volume of magma drained from the dyke intrusion as erupted onto the crater floor in the first few weeks of the eruption. The lava flows were observed to be emanating from cracks near the center of the crater (Andaru et al., 2021; Syahbana et al., 2019). Intermittent puffs originating from the summit continued until January 2018, after which seismic events and magmatic explosions became less frequent (Syahbana et al., 2019). Eruptive activity briefly increased in June–August 2018 with a second period of lava extrusion, before slowly dying down with the last explosive event happening on 13 June 2019 (Global Volcanism Program, CVGHM press-release 16 July 2020 Sennert, 2020; Syahbana et al., 2019).

On 21 November 2017, CVGHM started using a miniaturized Multiple Gas Analyzer System (multi-GAS) attached to an Uncrewed Aerial Vehicle (UAV) to obtain measurements of CO₂, SO₂, H₂S, and water vapor from the plumes. Magmatic gas, specifically CO₂, was detected 9 hr before the phreatomagmatic explosion on 21 November 2017. This was seen as a significant indicator of unrest (Syahbana et al., 2019). Notably, SO₂ emissions remained below the detection threshold (~0.05 ppmv) on November 21 but were detected the next day at a rate of 660 tonnes per day (Syahbana et al., 2019). The lack of magmatic gases, in particular SO₂, from observations before 21 November 2017, has been attributed to extensive scrubbing by the hydrothermal system (Syahbana et al., 2019; Symonds et al., 2001).

A puzzling aspect of this eruption and the preceding unrest is the lack of deformation, detected by InSAR or GPS, between the dyke intrusion and the start of the eruption. This could indicate that a long-lived, highly compressible magma reservoir was already present at depths shallower than 10 km. The compressibility, caused by the exsolution of volatiles from silicate melt (Kilbride et al., 2016; Wong & Segall, 2020), allows the reservoir to change its volume in response to pressure perturbations, reducing the magnitude of deformation observed at the surface (Kilbride et al., 2016; Yip et al., 2022). Alternatively, magma ascent to the summit could have been too localized to be detected by distant GPS stations and too rapid to be detected with satellite InSAR. However, several high-resolution SAR acquisitions were made over Agung before the eruption, which help to fill gaps in

Table 2

Summary of Synthetic Aperture Radar (SAR) Data With Satellite Name, Orbital Track Number, Number of Acquisitions, Number of Interferograms Used for MTI, Image Resolution (Across Track (i.e., Slant Range) and Along Track (i.e., Azimuth)), and Angle-Of-Incidence Over the Crater Floor

Satellite (mode ^a)	Track	Number of acquisitions	Interferograms in network	Resolution range × azimuth [m]	Angle-of-incidence [°]
CSK (spot)	07 (asc.)	20	66	0.32 × 0.70	29.6
CSK (spot)	05 (dsc.)	23 ^b	48	0.31 × 0.70	27.0
TSX (spot)	35 (asc.)	3	3	0.91 × 1.27	34.8
TSX (spot)	111 (asc.)	3	3	0.91 × 1.27	51.0
S1 (TOPS)	156 (asc.)	24	80	2.33 × 14.0	34.3
S1 (TOPS)	35 (dsc.)	23	71	2.33 × 14.0	39.0

Note. TSX data and interferograms were not used for MTI processing.

^aspot = spotlight; TOPS = Terrestrial Observation through Progressive Scans. ^bOnly 16 connected by coherent interferograms.

the progression from unrest to eruption and clarify the relation between the flank dyke intrusion and the shallow subsurface.

3. High-Resolution InSAR Measurements

Satellite InSAR allows us to measure surface displacement in the satellite line-of-sight (LOS) over a large area and thereby provides observations outside of the coverage of ground monitoring instruments. Current SAR satellites are able to make repeat observations within 16 days (e.g., TSX: 11 days, Sentinel-1: 6 or 12 days, CSK: 1–16 day(s)) and at spatial resolution of <5 m (e.g., TSX: 0.35 m range–0.2 m azimuth, Sentinel-1 2.3 m range–14 m azimuth, CSK: 0.3 m range–0.7 m azimuth). This allows us to monitor deformation events that are localized in space with a high temporal resolution. Time series analysis of volcano deformation can also be performed by using multiple acquisitions from the same satellite and look direction using methods collectively called MTI (e.g., Hooper, 2008). MTI can be used to track displacement rates as slow as ~1 mm/year (Lee et al., 2012; Li et al., 2021).

3.1. Data Selection and Processing

Through the CEOS Volcano Demonstrator Project we were able to access high-resolution SAR data, including CSK and TSX acquisitions in spotlight mode from 2017. We also analyze freely available data from Sentinel-1 acquired in Terrestrial Observation with Progressive Scans (TOPS) mode. The resolution, number of acquisitions, and angle-of-incidence over the crater floor are shown in Table 2. Sentinel-1 made 12-day repeat observations from both ascending and descending orbits, whereas CSK and TSX did not have fixed acquisition strategies, and repeat intervals ranged between 1 and 128 days in spotlight mode over Agung. A detailed description of the acquisition dates and perpendicular baselines is given in Table S1. The data were processed using GAMMA (Werner et al., 2000) at full resolution (see Table 2). In total, we processed 20 CSK ascending, 23 CSK descending, 24 Sentinel-1 ascending, 23 Sentinel-1 descending, and 6 TSX ascending (evenly divided 3-3 over two tracks) acquisitions with a view of the crater floor (see Table 2). High coherence interferograms (partially) spanning the pre-eruptive unrest period, from each data set are shown in Figure 4. In Figures 4a and 4b, fringes can be seen over most of the crater floor, even in the noisy less coherent areas. These areas are affected by signal overlay caused by the steep crater walls and only very small perpendicular baseline (≤ 25 m) interferograms are coherent in the signal overlay affected areas. On 25 November 2017, magmatic eruptions covered the crater floor in lava, making continued displacement analysis with InSAR impossible due to loss of coherence (Dietterich et al., 2012; Dualeh et al., 2021; Zebker et al., 1996).

Phase coherence between images is required for interferometry and is affected by the temporal and geometric (perpendicular) baselines (Hanssen, 2001). We selected images to provide good coherence at the summit. CSK ascending interferograms were most impacted by the perpendicular baseline (B_{\perp}), with $B_{\perp} > 300$ m resulting in incoherent interferograms. The quality of CSK descending interferograms varied significantly; therefore, image

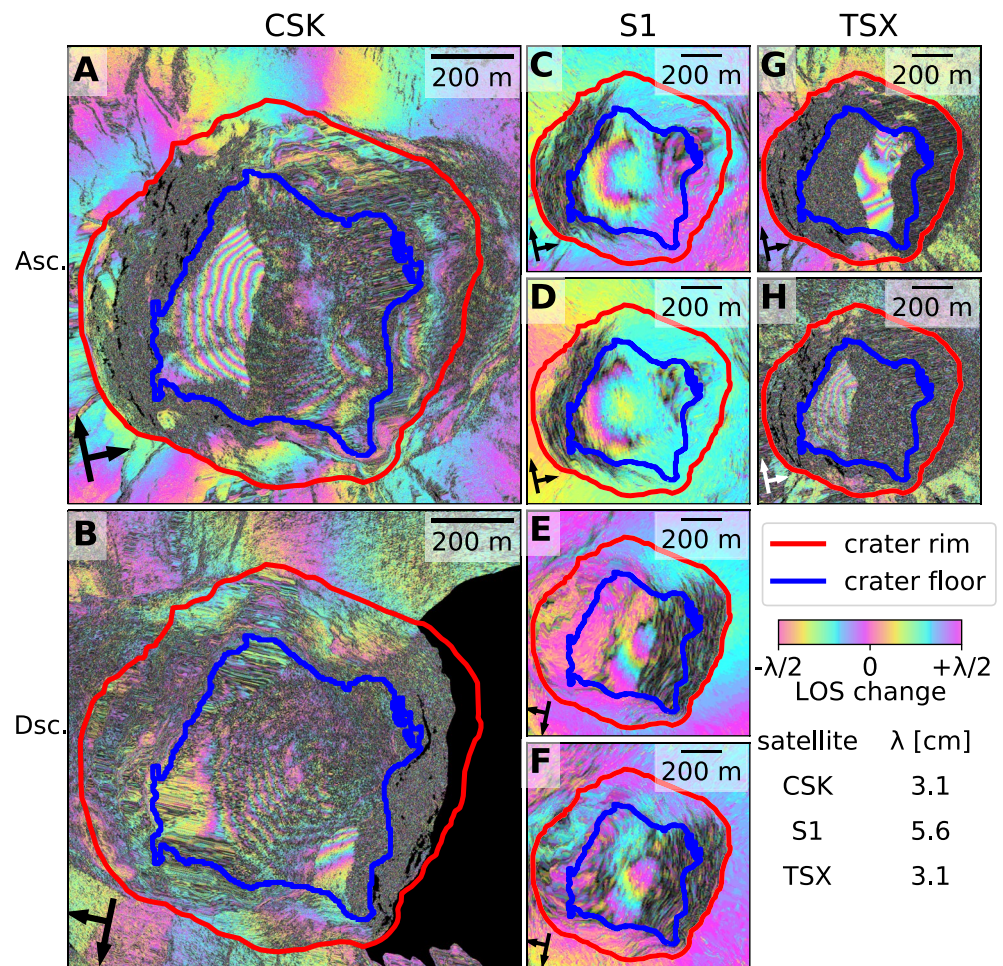


Figure 4. Interferograms showing line-of-sight (LOS) decrease on the crater floor. (a) CSK ascending from 18 April to 16 November 2017. (b) CSK descending from 13 May to 9 November 2017. (c) Sentinel-1 ascending from September 18, to 30, 2017. (d) Sentinel-1 ascending from 30 September to 12 October 2017. (e) Sentinel-1 descending from 21 September to 3 October 2017. (f) Sentinel-1 descending from 3 to 15 October 2017. The Sentinel-1 interferograms are sequential. (g) TSX ascending (track 111) from 28 September to 20 October 2017. (h) TSX ascending (track 35) from 29 September to 9 November 2017. Black/white arrows indicate the satellite orbit and look direction.

pairs with $B_{\perp} < 300$ m were visually inspected for coherence over the crater floor. Out of 23 acquisition dates and 91 image pairs with $B_{\perp} < 300$ m, only 16 acquisition dates and 48 image pairs were selected. The perpendicular baseline of Sentinel-1 ascending and descending data is tightly controlled such that $B_{\perp} < 200$ m and does not affect coherence significantly. Temporal baselines longer than 48 days caused loss of coherence in the Sentinel-1 interferograms, limiting the number of image pairs to 80 and 71 for Sentinel-1 ascending and descending, respectively. The two TSX tracks with a view of the crater floor each only have three acquisitions, making three image pairs, which provide useful constraints on the timing of deformation but are insufficient for time series processing. Additionally, these acquisitions started after the onset of deformation in the crater, not capturing the full evolution of the deformation signal and highlighting the importance of data acquisition as part of background missions.

3.2. Digital Elevation Model

DEMs are used in differential InSAR to remove the contribution of topography created by the geometric (perpendicular) baseline separating the satellite acquisitions. DEMs are also used to georeference the resulting interferograms. Automated processing is commonly done at ≥ 30 m resolution using global 30–90 m resolution DEMs (e.g., LiCSAR (Lazeký et al., 2020) 90–110 m using 90 m Shuttle Radar Topography Mission (SRTM) DEM

(Farr et al., 2007), ARIA 90–110 m using 30 m SRTM DEM (Bekaert et al., 2019), and FLATSIM 30 or 100 m using 30 m SRTM DEM (Thollard et al., 2021)), but high-resolution InSAR benefits from DEMs with ≤ 30 m resolution (Du et al., 2017). Steep slopes (including deep craters) and frequent cloud cover, both present at tropical stratovolcanoes, can result in lower accuracy and data gaps in DEMs (Ebmeier et al., 2013; Rodriguez et al., 2006); therefore, it is important to assess the quality of the DEMs used.

We tested four different DEMs: (a) the free and open-source SRTM 90 m DEM, (b) the SRTM 30 m DEM, (c) a 9 m DEM created from TSX data (acquired from April 2011 to February 2012) using stereo-radargrammetric mapping (De Oliveira et al., 2011; Raggam et al., 2010), and (d) a mosaic of the 9 m TSX DEM (up-sampled to 5 m) for which we update the summit area using a 5 m DEM created from commercial WorldView-3 (WV3) along-track panchromatic stereo pairs collected on October 11 and 29 October 2017, using the NASA Ames Stereo Pipeline, following the workflow described in Shean et al. (2016). Due to the steep crater walls and strong shadowing effect, point clouds from both image dates with slightly different imaging angles were used to create a high-resolution DEM of the summit crater and upper flanks of the volcano. Farther downslope the presence of vegetation caused significant incoherence in the results of the WV3 models. Therefore, the 9 m TSX DEM was used to expand the footprint of the merged DEM to encompass the lower flanks and surrounding area. The TSX and WV3 DEMs were co-registered to align and minimize positional biases and then merged using a priority blending length integer which prioritized valid pixels in the WV3 DEM and used the TSX DEM to fill and expand areas with no pixel values and blend the two only at their boundaries (Beyer et al., 2018, 2019). We processed one CSK ascending interferogram from April 18 to 16 November 2017, and one Sentinel-1 ascending interferogram from 18 September to 12 October 2017, to assess the influence of DEM resolution and height accuracy over the summit crater. The TSX + WV3 5 m DEM provides the most accurate georeferencing and allows for InSAR processing at the native resolution of the SAR data and is therefore used for topographic correction during time series processing.

3.2.1. Influence of DEM Resolution

The resolution at which the SAR data are processed determines the maximum lateral displacement gradient (i.e., meters of displacement in LOS divided by meters laterally on the surface) which we can resolve. Displacement cannot be resolved when the displacement between two adjacent pixels exceeds $\frac{1}{2}$ of the radar wavelength (Klees & Massonnet, 1998; Massonnet & Feigl, 1998), and phase unwrapping algorithms are generally limited to phase differences $< \pi$ (Yu et al., 2019, and references therein), equivalent to $\frac{1}{4}$ of the radar wavelength. Assuming the deformation at the summit of Agung is limited to the ~ 530 m wide crater floor and is largest in the center, we would be able to resolve and unwrap 2.3 and 4.1 cm of LOS deformation for X band (wavelength: ~ 3.1 cm, e.g., CSK and TSX) and C band (wavelength ~ 5.6 cm, e.g., Sentinel-1), respectively, at a resolution of 90 m. These numbers increase to 6.8 and 12.4 cm at 30 m resolution, and 41.1 and 74.2 cm at 5 m resolution. Coherence loss due to geometric, Doppler-centroid, temporal, and volume scattering decorrelation as well as thermal noise will cause spatial under-sampling of the deformation phase to occur below these theoretical limits (Hanssen, 2001). In Figures 5a and 5e, processed at 30 and 90 m, respectively, no fringes are useable due to under-sampling of the phase signal. We can see that at 10 m resolution for CSK (Figure 5b) and 30 m resolution for Sentinel-1 (Figure 5g) the fringes are barely distinguishable. In Figures 5c–5d and 5g–5h the fringes are well defined and clearly distinct from each other, showing that high-resolution (< 10 m) DEMs are needed to resolve the deformation inside the crater.

Oversampling the DEM such that it more closely matches the resolution of the SAR data can improve image quality (Small et al., 1998). We can see the effect of DEM oversampling in Figures 5b and 5g when compared to Figures 5a and 5f, respectively. Figures 5g and 5h show that there is little difference between using a high-resolution DEM or oversampling a DEM to the desired resolution. However, when the oversampling factor is too large, co-registration between the DEM and the SAR image fails.

3.2.2. Influence of DEM Accuracy

Georeferencing using an out-of-date or otherwise inaccurate DEM can lead to mis-interpretation of the deformation data by stretching and moving the image. Differences between the DEM and the actual topography will increase the contribution of perpendicular baseline effects, which are used to estimate changes in topography (in absence of deformation) (Albino & Biggs, 2021; Ebmeier et al., 2012; Poland, 2014) and increases perpendicular baseline related nuisance terms during MTI (Hooper et al., 2007). The summit crater area in the 9 m TSX

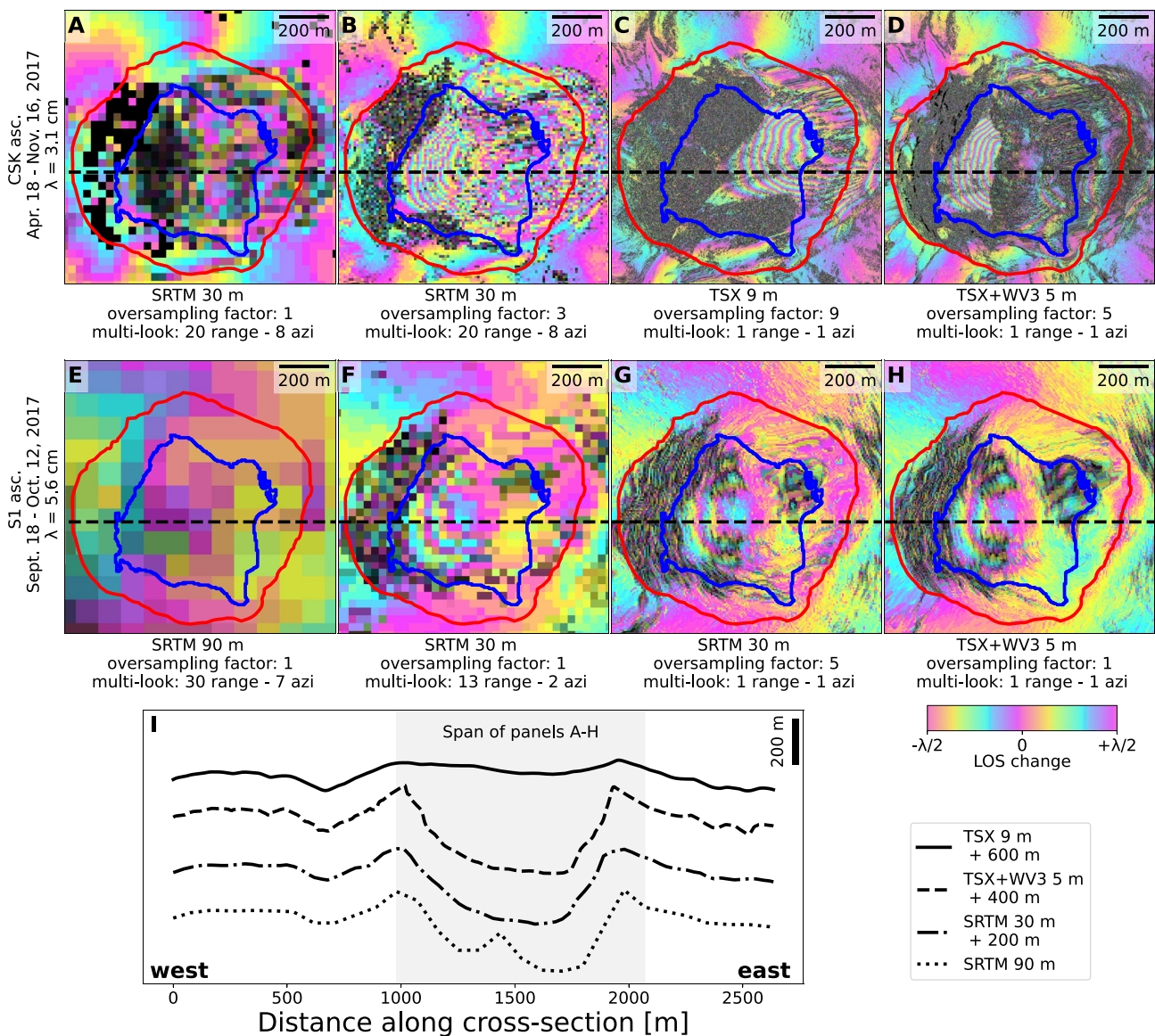


Figure 5. Effect of resolution and DEM quality on InSAR processing and interpretation. A–D: CSK ascending interferogram from 18 April to 16 November 2017. (e–h) Sentinel-1 interferogram from 18 September to 12 October 2017. DEM used for processing, DEM oversampling factor, and SAR multi-looking factors in range and azimuth (azi) are listed below panels (a–h) (TSX + WV3 5 m refers to the mosaic of the TSX and WorldView-3 DEMs sampled at 5 m resolution). Panel I shows a cross-section of the DEMs (vertically offset from each other for clarity) along the dashed line in (a–h) (no vertical exaggeration). The gray-shaded region shows the extent of panels (a–h).

DEM only goes down 40–50 m from the crater rim to the crater floor and does not show the 200–400 m deep crater that is present in the other DEMs (Figure 5i) and that is observed with UAV-based photogrammetry of the summit prior to the 2017 eruptions (Andaru et al., 2021). This flat summit is likely the result of interpolation over gaps created by shadow and signal overlay areas in the TSX data used. When georeferencing, this discrepancy causes the deformation signal to appear stretched and greatest on the eastern edge of the crater floor (Figure 5c), similar to the deformation signal shown in Poland et al. (2020) and Poland and de Zeeuw-van Dalfsen (2021). In reality, the deformation signal is greatest in the center of the crater floor and is bounded to the west by the crater walls (Figure 5d).

Using the 9 m TSX DEM distorted the deformation signal in the CSK ascending data such that it appeared on the eastern side of the crater (Figure 5c), where it would be wrongly attributed to the fumarolic field. Similarly, the deformation signal in the CSK descending data was distorted such that it appeared on the southern crater

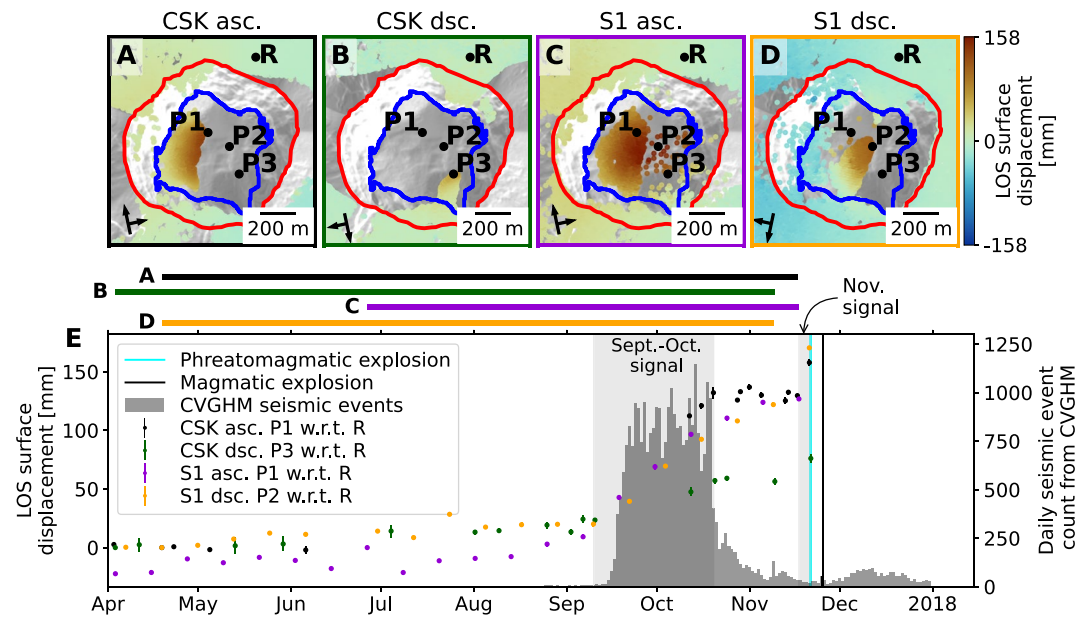


Figure 6. InSAR displacement maps and time series over the summit of Agung. (a–d) StaMPS LOS surface displacement from (a) CSK ascending 18 April to 16 November 2017, (b) CSK descending 3 April to 9 November 2017, (c) Sentinel-1 ascending 26 June to 17 November 2017, (d) Sentinel-1 descending 18 April to 8 November 2017. Arrows show satellite flight and look direction. (e) Time series of LOS surface displacement of point P1 (for CSK and Sentinel-1 ascending), P2 (for Sentinel-1 descending), and P3 (for CSK descending) with respect to point R. Error bars indicate 1σ uncertainty from scatterers within a 25 m radius of R. Also shown are the CVGHM daily seismic event count in gray as well as the phreatomagmatic (cyan) and magmatic (black) explosions on 21 and 25 November 2017, respectively. The September–October and November deformation periods are shown in gray. The time spanned by (a–d) is shown by the colored lines above (e).

wall, where it might be wrongly attributed to artifacts caused by expected DEM inaccuracies related to the steep topography of the crater wall. Using the TSX + WV3 5 m DEM, interferograms from multiple satellites/tracks are georeferenced such that the deformation signals appear largest at the center of the crater floor (Figures 5d and 5h).

3.3. Time Series Processing

We performed time series InSAR using Stanford Method for Persistent Scatterers/Multi-Temporal InSAR (StaMPS/MTI) small-baseline processing (Hooper et al., 2012) using parameters appropriate for the high resolution of our input data (e.g., no or limited data sub-sampling and small window sizes for unwrapping and filtering). The StaMPS parameter files are made available on the Zenodo repository (see –Data Availability Statement). This resulted in 1,069,527 persistent scatterers (PS) across both CSK and Sentinel-1 tracks, of which 28,523 are on the crater floor. CSK and S1 data provide 87% and 13% of PS, respectively, shifting to 93% and 7% of PS on the crater floor. No external information was used to remove the effects of atmospheric delay, as our signal of interest has a much smaller footprint than can be resolved with the weather models used for these corrections (Parker et al., 2015; Yip et al., 2019). Signals that are spatially correlated but temporally uncorrelated (e.g., stratified atmosphere), and signals that are uncorrelated in space and time (e.g., turbulent atmosphere), are estimated and removed by means of filtering as part of StaMPS/MTI processing (Hooper, 2008).

4. Results

Figures 6a–6d show LOS surface displacement maps for CSK ascending (from 18 April to 16 November 2017), CSK descending (from 3 April to 9 November 2017), Sentinel-1 ascending (from 26 June to 17 November 2017), and Sentinel-1 descending (from 18 April to 8 November 2017). The displacement appears to be greatest in the center of the crater and approximately radially symmetric. Both the ascending and descending orbits show surface displacement toward the satellite of similar magnitudes over the same area, which indicates the signal is primarily

uplift. We do not have data covering the entire crater floor because the steep terrain creates shadow regions and distortion/decorrelation in regions of layover and foreshortening.

Figure 6e shows time series of LOS displacement of points on the crater floor: P1 (for CSK ascending and Sentinel-1 ascending), P2 (for Sentinel-1 descending), and P3 (for CSK descending), with respect to reference point *R* on the summit just north of the crater (see Figures 6a–6d for the location of P1–3 and *R*). All persistent scatterers within a 25 m radius of P1–3 and *R* are considered to obtain a robust value with the estimation of data variability taken from the 25 m radius area around *R*. The time series show two periods of displacement; the first from September to mid-October, and the second from 17 to 21 November 2017. We will refer to these time-separated displacement signals as the September–October signal and the November signal, respectively. The Sentinel-1 ascending time series shows an upward trend in displacement from August 2017, but the magnitude of this potential early displacement signal is too small ($\leq \frac{1}{2}$ fringe) to be confidently assessed.

4.1. The September–October Signal

From September to mid-October, 10–15 cm of LOS displacement was observed (see Figure 6e). All time series suggest that displacement starts in early to mid-September. The fastest LOS displacement rates occurred from late September to early October, coincident with the peak in seismic event rate, and measured 5.7 ± 0.15 mm/day in LOS (equivalent to 10.1 ± 0.27 mm/day assuming pure uplift (i.e., $\frac{\Delta LOS}{\cos(\phi)}$, where ϕ is the angle-of-incidence)) for the Sentinel-1 ascending track. The CSK descending data only capture the edge of the displacement signal and, therefore, the magnitude of displacement is significantly lower. Deformation slows down or halts completely between late October and early November, in concert with the decline in seismicity. Between early September and mid-November, a maximum of 154 ± 2 mm of LOS displacement (equivalent to 273 ± 3 mm assuming pure uplift) was observed in the Sentinel-1 ascending track.

The displacement is completely confined to the crater floor and covers at least 400-by-400 m, or 0.16 km²; however, it is reasonable to assume that displacement also occurs in the obscured area of the crater, especially when considering the fringes observed with TSX track 35 (see Figure 4g), possibly increasing the deformation footprint to the entire crater floor (approximately 530-by-530 m or ~ 0.28 km²).

4.2. The November Signal

The second pulse of displacement is visible in the CSK ascending and Sentinel-1 descending time series (see Figure 7), which both have their last useful acquisition on 20 November, about 11 hr before the phreatomagmatic eruption, and CSK descending, for which the last acquisition was 40 min after the phreatomagmatic eruption. Since the November signal is only present in the last acquisition of the time series, we manually inspected the individual interferograms to ensure that this is not a processing or other artifact. The CSK ascending interferogram (Figure 7b) shows 2–3 fringes toward the center of the crater floor, confirming that the November signal is not just an artifact of the StaMPS/MTI processing. The November signal is also present in the CSK descending and Sentinel-1 descending data, where it is best seen in the displacement of the persistent scatterers (see Figures 7c and 7d). The signal occurs in approximately the same location as the September–October signal, but both the footprint and magnitude of the November signal are smaller at 300-by-200 m and 3–5 cm, respectively. With the help of interferograms showing no deformation (see Figure 7a), we are able to constrain the deformation period to within 4 days at most and 11 hr at the least before the onset of the eruption.

5. Deformation Source Modeling

5.1. Inversion Method

We use Geodetic Bayesian Inversion Software (GBIS) (Bagnardi & Hooper, 2018) to model the source of the displacement signal. GBIS uses elastic half-space models (e.g., point/Mogi (1958), spherical (McTigue, 1987), planar opening (Okada, 1992), penny-shaped crack (Fialko et al., 2001)) to estimate the position and geometry of the source from surface displacement data and a-priori constraints. We model the September–October signal and the November signal separately. We are introducing a number of simplifications by modeling the displacement in elastic half-space. In reality, we do not expect the (shallow) subsurface of the volcano to behave purely elastically (Head et al., 2021; Hickey et al., 2016; Hickey & Gottsmann, 2014; Holohan et al., 2017; Masterlark, 2003), and

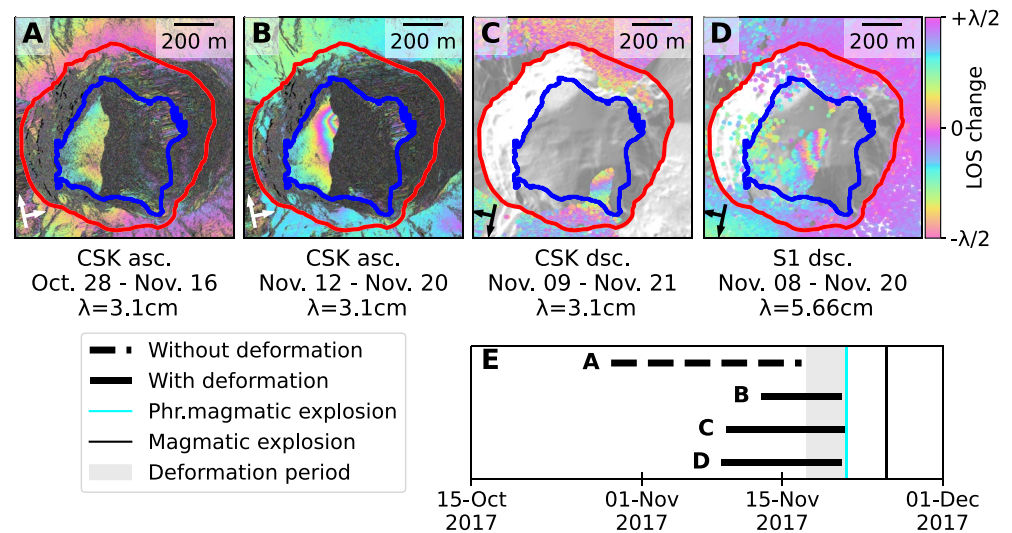


Figure 7. Observations of the November signal from interferograms and MTI. (a and b) CSK ascending interferograms used to constrain the November signal. (c and d) Re-wrapped StaMPS displacement over the November signal for CSK descending and Sentinel-1 descending. The white/black arrows show the orbit and look direction of the satellites. (e) Period spanning interferograms. The gray-shaded region indicates the constraint on the deformation period given by the interferograms. The cyan and black vertical lines show the phreatomagmatic and magmatic explosions, respectively.

there is a possibility that steep relief (e.g., areas outside of the crater floor and the crater walls) influence our results (Cayol & Cornet, 1998; Masterlark, 2003; Williams & Wadge, 1998). Additionally, the simple source geometries we selected (i.e., point, sphere, planar opening, or penny-shaped crack) will only give a simplification of the approximate shape and location of the source.

GBIS model inversions start with an initial set of model parameters, which can be arbitrarily chosen or previously estimated through a direct-search method (Bagnardi & Hooper, 2018). The initial set of model parameters is used to initiate the iterative process of calculating the likelihood of the set of model parameters given the data used for the inversion. Additionally, the model parameters may be constrained within bounds. For these bounds, we chose a source position within the crater (± 1000 m from the crater center) and at 0–1500 m depth (see Table S3 in Supporting Information S1). Additionally, for each satellite track, a uniform offset value is estimated and removed such that the errors have zero mean.

For the model inversion of the September–October signal, we used the LOS displacement of the persistent scatterers of the CSK and Sentinel-1 tracks shown in Figures 6a–6d. For the November signal, we used StaMPS/MTI displacement of CSK ascending (16–20 November 2017), CSK descending (9–21 November 2017) and Sentinel-1 descending (8–20 November 2017). The total number of persistent scatterers is of the order 10^6 , which is too large for the inversion, requiring data reduction. Previous studies have achieved this by sub-sampling on a uniform grid (e.g., Pritchard et al., 2002), on a circular grid where sampling becomes less dense away from the center (e.g., Johanson & Bürgmann, 2005), via a quadtree algorithm (Bagnardi & Hooper, 2018; Jónsson et al., 2002), resolution-based sub-sampling (Lohman & Simons, 2005), or a defined region of interest (Yunjun et al., 2021). Since our signal of interest is confined to the crater floor, we sub-sampled with a 200 m uniform grid outside of the crater floor and used a 25 m uniform grid on the crater floor. We defined the crater floor as the area which has a slope of $\leq 45^\circ$ (see Figure S1 B in Supporting Information S1). This sub-sampling reduced the input data from $\sim 10^6$ persistent scatterers to 1,345 grid-cells. We applied a median filter to the LOS surface displacement of the persistent scatterers contained in each grid-cell and mapped that to the mean position of the persistent scatterers within each cell (see Figures S1 D,F,H,J in Supporting Information S1).

To calculate errors and error significance during the model inversion, a variance-covariance matrix of the InSAR data is required. This was created by fitting an exponential variogram to the data outside the crater (i.e., without a deformation signal). We assume that the noise characteristics of the StaMPS results from the crater floor and from the data outside the crater are similar, especially over distances shorter than 400 m (i.e., the extent of the signal on the crater floor). The exponential variogram was then applied to the distance matrix of the sub-sampled

data to create the variance-covariance matrix. (See supplemental material for details on the variance-covariance matrix, and an overview of a-priori bounds.)

We performed model inversions using five different geometries: (a) point source (Mogi, 1958), (b) finite sphere (McTigue, 1987), (c) penny-shaped crack (Fialko et al., 2001), (d) prolate ellipsoid (Yang et al., 1988), and (e) a rectangular opening (sill/dyke) (Okada, 1992). These models neglect the effect of topography, which can affect the inversion (Williams & Wadge, 1998). However, our signal of interest is on the relatively flat crater floor where the 1σ height variation of the persistent scatterers is 28 m. We let GBIS perform 5×10^5 simulations for each of the tested geometries, and we re-ran 1×10^6 simulations for the model geometries that did not converge to a single solution after the initial 5×10^5 runs.

5.2. Model Selection and Limitations

We used two statistical tests: (a) the Overall Model Test (OMT) (Teunissen, 2006) and (b) the Akaike Information Criterion (AIC) (Akaike, 1974) to assess the models for goodness of fit considering both data (co)variance and the degrees of freedom for each of the models. Both test statistics were calculated under the assumption that the residuals are normally distributed.

The OMT test uses test statistic T , which is given by the weighted sum of squared residuals:

$$T = \hat{e}^T Q_{yy}^{-1} \hat{e}, \quad (1)$$

where \hat{e} are the residuals ($\hat{C}e = O - M$, where O are the observations and M is the optimal model solution) and Q_{yy} is the covariance matrix of the observations made using an exponential variogram fitted to the sub-sampled data. Test statistic T follows a $\chi^2(N_{df}, 0)$ distribution, where N_{df} is the degrees of freedom of the model (Teunissen, 2006). The critical value $K_{N_{df},\alpha}$ is given by the inverse cumulative probability density function for a $\chi^2(N_{df}, 0)$ distribution at the required level of significance α , in our Case 0.05. Models that fail the OMT should not be considered and when multiple models pass the OMT, the model solution with the lowest normalized test statistic (defined as $\frac{T}{K_{N_{df},\alpha}}$) is the desired model (Toodesh et al., 2021).

The AIC values can be computed with:

$$AIC = n \ln \frac{\chi^2}{n} + 2k, \quad (2)$$

where n is the number of sub-sampled data points, χ^2 is the weighted sum of squared residuals (as for T) and k is the number of parameters used in the inversion plus one (D. Anderson & Burnham, 2004; Johanson & Bürgmann, 2005) (for point source $k = 9$, for spherical source and penny-shaped crack $k = 10$, and for ellipsoidal source and planar opening $k = 13$). The model with the lowest AIC score is considered the best performing model out of the models tested against the same data set (Akaike, 1974; D. Anderson & Burnham, 2004).

5.3. Model Results

Of the five tested geometries for the September-October signal, the spherical and prolate ellipsoid converged to unrealistic solutions and were therefore removed from consideration: the spherical geometry converged to radius \gg depth and the prolate ellipsoid had axis ratios ($\frac{\text{minor}}{\text{major}} < 0.05$) and a multi-modal distribution of normalized pressure change solutions. The point source geometry barely passed the OMT ($\frac{T}{K_{\text{dof},0.05}} = 0.9957$) and performed significantly worse than the other remaining geometries; for these reasons, we also exclude the point source from further consideration.

The results for the two remaining geometries (penny-shaped crack and rectangular sub-horizontal sill) are presented in Table 3 and Figure 8. The optimal solution for the penny-shaped crack is located centrally within the crater, 165 m below the surface with a radius of ~ 200 m. The optimal solution for the rectangular sub-horizontal sill is similarly located centrally within the crater, with side-lengths of ~ 300 m. The rectangular sub-horizontal sill has a top edge depth of 84 m and dips 20° toward SW. The estimated volume change of the penny-shaped crack and the rectangular sub-horizontal sill are 14×10^3 and $19 \times 10^3 \text{ m}^3$, respectively. Both geometries pass the OMT at the 0.05 level of significance. Visually, the penny-shaped crack solution fits the descending orbit data

Table 3

GBIS Optimal Solutions for a Penny-Shaped Crack and Sub-Horizontal Sill for the September-October Signal and November Signal

Parameter	Penny-shaped crack September-October	Sub-horizontal sill	
		September-October	November
Easting [m]	−54	34	51
Northing [m]	−33	87	67
Depth [m]	165	84	57
Radius [m]	198	–	–
$\frac{\Delta P}{\mu} \cdot 10^{-4}$	9.05	–	–
Length [m]	–	316	260
Width	–	313	153
Dip [°]	–	−20	−16
Strike [°]	–	306	328
Opening [cm]	–	19.9	7.8
T	1349.9	1257.4	720.9
$T/K_{N_{dir},0.05}$	0.95	0.89	0.70
AIC	26.9	−61.5	−251.6 ^a

Note. $T/K_{N_{dir},0.05}$ is the normalized OMT test statistic equal to $\hat{e}Q_{yy}^{-1}\hat{e}'/K_{N_{dir},\alpha=0.05}$. Easting and Northing are relative to the approximate center of the crater (i.e., longitude: 115.508007, latitude: −8.342826) and refer to the center of the penny-shaped crack and the middle of the shallow edge of the sub-horizontal sill. Pressure change is normalized with the shear modulus μ .

^aOnly meaningful in relation to other models fit to the same input data.

better (see gray dashed ellipses in Figures 8r and 8t), with little difference in the ascending orbit data; however, both normalized OMT scores and AIC values suggest that the rectangular sub-horizontal sill outperforms the penny-shaped crack. The actual source will probably share attributes with both over-simplified model solutions that point to a shallowly dipping or horizontally oriented source that extends to less than 200 m below the surface. The estimated pressure change of $0.9 \times 10^{-4}\mu$ (where μ is the shear modulus) could be an overestimation as the models do not allow for source boundary expansion to reduce overpressure (Gregg et al., 2013). Additionally, it is possible that these model solutions only represent the top-surface of the actual pressure source (Yun et al., 2006).

For the November signal, we inverted for a sub-horizontal sill to compare against the solutions of the September-October signal (see Figure S2 in Supporting Information S1 for comparison of data, model, and residuals for the November signal). The optimal model solution after 5×10^5 iterations are shown in Table 3. The location, orientation, and length of the best-fitting sill for the November signal are similar to the best-fitting sill for the September-October signal. In contrast, the width and opening are significantly smaller. The two sill models could both be expressions of the same reservoir, the difference in width could indicate that only part of the reservoir was pressurized in November compared to September-October, while the difference in opening could indicate a smaller change in reservoir pressurization or be the result of limited data coverage on the northeastern part of the crater floor (see Figure 4). The best-fit sill sources for the September-October signal and the November signal have approximately 1 order of magnitude difference in source volume (2.0×10^6 and 0.3×10^6 m³, respectively). We expect the pressure change in a volume constant source (like the penny-shaped crack) to show a similar magnitude change.

6. Discussion

6.1. Intra-Crater Deformation: The Missing Piece of the Dynamics of Agung Puzzle

Our results indicate that two distinct phases of deformation on the crater floor of Agung volcano took place prior to its eruption onset on 21 November 2017. The first stage (the September-October signal) occurred together with the unrest caused by a flank dyke intrusion between Agung and Batur volcanoes. We attribute the September-October deformation to the pressurization of a shallowly dipping/horizontal, flat-topped source located high within the edifice of the volcano, within 200 m of the crater floor.

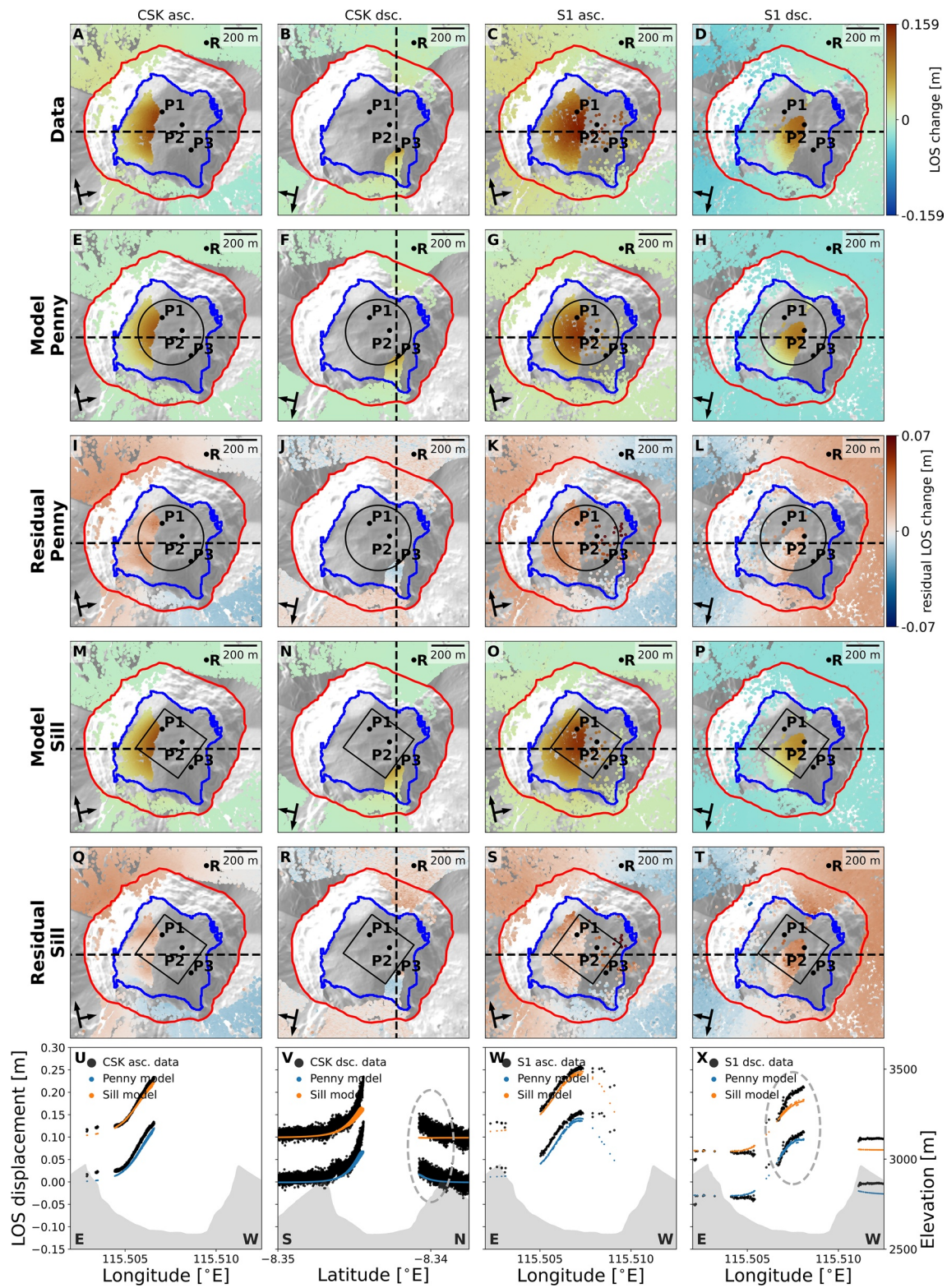


Figure 8.

Fitting the observed deformation to one of the mechanisms described in Section 2.1 is not trivial. It is possible for magma to intrude at such shallow depths (e.g., Cordon Caulle, Chile, and Usu, Japan, Castro et al., 2016; Delgado et al., 2019; Tobita et al., 2001). However, we propose a shallow hydrothermal system as the source of

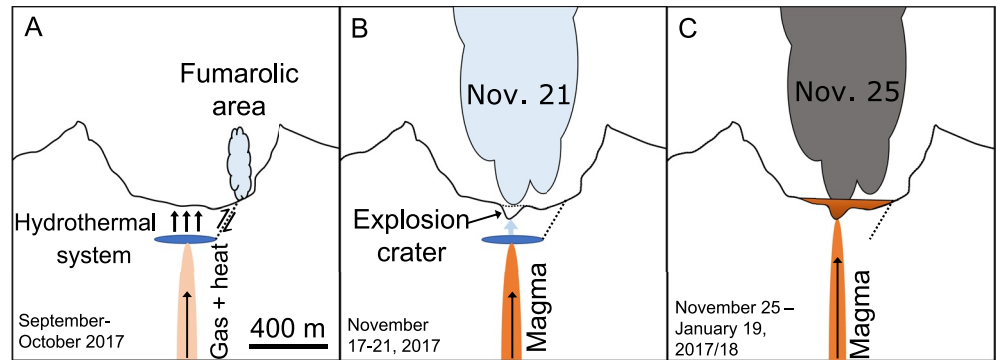


Figure 9. Temporal evolution of events at the summit of Agung. Panel A shows the first period of intra-crater deformation spanning mid-September to mid-October 2017, where gases and heat ascended from a flank dyke intrusion between Agung and Batur, pressurizing the hydrothermal system at the summit opening/widening pathways to the fumarolic field and increasing fumarolic activity. Panel B shows the second period of intra-crater deformation spanning November 17–21, 2017. Here, magma has ascended to shallow depths and is interacting with the hydrothermal system, eventually triggering a phreatomagmatic explosion on 21 November 2017, which created an explosion crater in the center of the larger summit crater floor (Syahbana et al., 2019). Panel C shows the period where magma reached the surface to flood the crater floor, starting with a magmatic explosion on 25 November 2017 (Syahbana et al., 2019).

deformation based on: (a) the lack of magmatic gases emitted prior to eruption, pointing to extensive scrubbing by a hydrothermal system (Syahbana et al., 2019; Symonds et al., 2001), (b) the increased activity of the fumarolic field located in the crater during September–October 2017, (c) the shallow depth of the modeled source (<200 m) and the lack of temperature anomalies at the summit until late 2017, which exclude the presence of a persistent high-melt-fraction magma body (possibly remnant from the 1963 eruption) in the shallow subsurface, (d) migration of seismic activity from October–November, attributed to magma ascent (Sahara et al., 2021; Wellik et al., 2021), lagging behind the intra-crater deformation starting in September, and (e) the difference in volume change associated with the September–October deformation ($\sim 1 \times 10^4 \text{ m}^3$) and the erupted magma from 25 November to 18 December 2017 ($27 \times 10^6 \text{ m}^3$) (Andaru et al., 2021). While sub-surface volume change and erupted volume are not expected to be equal (Kilbride et al., 2016; Yip et al., 2022), the orders of magnitude difference points to differing sources/mechanisms. The volume change of the September–October source is therefore not related to magma transport, but rather to a perturbation of the shallow hydrothermal system.

We hypothesize that the hydrothermal system was perturbed and became pressurized by the injection of magmatic fluids supplied from depth during the flank dyke intrusion (Figure 9a). The full extent and complexity of the hydrothermal system cannot be assessed from these observations and modeling efforts alone. We do not see any subsidence caused by pressure release from any of the phreatic explosions that occurred in September–October 2017. These subsidence signal could have been too small in magnitude to be observed, occurring mainly over the fumarolic field, which has poor data coverage, or a continued magmatic fluid influx may have maintained over pressure following the phreatic explosion. The deformation in the summit crater slowed or paused from mid-October to mid-November, in tandem with the decline in seismic activity and flank dyke intrusion rate over the same period (Albino et al., 2019; Syahbana et al., 2019). This could be explained by a reduction in the supply of magmatic fluids.

Prior to the onset of the eruption on 21 November 2017, we observe a second phase of deformation on the crater floor. The signal taking place during 17–21 November 2017 (4 days–11 hr before eruption onset), provides valuable insights into the underlying mechanism of deformation. There is compelling evidence that magma was ascending to shallow depths by this time as indicated by: (a) the onset of tremor on 12 November 2017 (Syahbana

Figure 8. Optimal analytical model solutions for the September–October signal. (a–d) Data used for model inversion and residual calculation, also shown in Figures 6a–6d. The dates spanning the observed LOS displacement of panels (a–d) are April 18–16 November 2017, 3 April–9 November 2017, 26 June–17 November 2017, and 18 April–8 November 2017, respectively. (e–h) LOS displacement for optimal penny-shaped crack solution. Black circle shows outline of optimal model (i–l) Residual LOS displacement (observations–model) for the penny-shaped crack model. (m–p) LOS displacement for optimal sub-horizontal sill solution. Black rectangle shows outline of the optimal sill model. (q–t) Residual LOS displacement (observations–model) for the sub-horizontal sill model. Points P1, P2, P3, and R refer to locations used in the time series plot in Figure 6. Black dashed line shows the line of cross-section for the bottom panels. Arrows show orbit and look direction. (u–x) cross-section of observed displacement (black), modeled displacement (blue and orange for penny-shaped crack and sub-horizontal sill (offset by +0.1 m), respectively) and elevation (gray) (no vertical exaggeration). Gray-dashed ellipses in R and T highlight differences in the optimal solutions of the penny-shaped crack and sill.

et al., 2019), (b) a migration of seismic activity from the site of the dyke intrusion to the summit of Agung from October to November 2017 (Sahara et al., 2021), (c) a change in the behavior of earthquake families from intrusive (before 12 November 2017) to eruptive (after 15 November 2017) (Wellik et al., 2021), and (d) Anomalous CO₂ gas detected on the morning of the eruption (Syahbana et al., 2019).

Given the multiple lines of evidence for magma movement toward the summit, it is likely that the November signal is the result of the interaction of the ascending magma with the hydrothermal system at the summit. We propose that the supply of heat and magmatic fluids rapidly increased the pressure on the hydrothermal system, leading to the November deformation signal and the phreatomagmatic explosion on 21 November 2017. By 25 November 2017, magma had ascended to the surface and started to emanate from cracks in the center of the crater floor (Andaru et al., 2021; Syahbana et al., 2019). This was close to the location of maximum surface displacement for both the September-October and the November deformation signals on the crater floor. By this stage, it is likely that at least part of the hydrothermal system had boiled away.

There is no evidence of edifice-wide deformation associated with either magma ascent or a shallow magma reservoir (Albino et al., 2019, 2020). Petrological studies based on the 1963 eruption identified a shallow magma storage zone at depths of 3–7 km (Geiger et al., 2018; Self & King, 1996). Either this reservoir was exhausted during the 1963 eruption and no longer exists, or the magma is so gas-rich (Syahbana et al., 2019) that it is highly compressible and the deformation is below the detection limit (Albino et al., 2019; Kilbride et al., 2016; Yip et al., 2022). Deformation associated with magma ascent is rarely observed and probably indicates that the ascent was rapid and occurred a few days before the onset of eruption (Wellik et al., 2021). Despite the lack of direct evidence of shallow magma movement, our observations suggest that precursory deformation signals do exist and can be detected using the right data at the right time.

6.2. Ascent and Storage of Magmatic Fluids in the Shallow Subsurface

Observations of localized deformation provide clues to the behavior of magma, hydrothermal fluids, and gases in the shallow subsurface. The ascent path of pressurized fluids is determined by the stress field, fluid rheology, strength of the surrounding rock, and any pre-existing structures (Albino et al., 2019; Benson et al., 2012; Gudmundsson, 2006; Hutchison et al., 2015; Lamur et al., 2017). Our observations prior to the 2017 eruption of Agung are similar to those made prior to the 2015 phreatic eruption of Hakone, Japan, where deformation was also caused by a shallow (~150 m) lens-shaped hydrothermal source driven by the injection of magmatic fluids and heat from depth (Kobayashi et al., 2018). A reduction in deformation rate a month before the eruption of Hakone was attributed to a reduction in the supply of magmatic fluids to the shallow hydrothermal system (Kobayashi et al., 2018). Kobayashi et al. (2018) additionally speculated that sealing of the pathways to the hydrothermal system caused a deceleration in the deformation rate, with deformation accelerating upon the penetration of the sealing layer in the days leading up to the eruption.

Shallow intrusions have led to the formation of trapdoor faults at several basaltic volcanoes (e.g., Sierra Negra, Galápagos (Jónsson, 2009; Jónsson et al., 2005); Piton de la Fournaise, Réunion Island (Q. Dumont et al., 2022)). At Agung, we see evidence for inflation of a ~300 m wide, sill-like source less than 200 m beneath the crater floor, yet we see no evidence of trapdoor faulting. At such a shallow depth, the source will interact with the free surface (Fialko et al., 2001) such that the orientation of maximum compressive strength curves up toward the free-surface and the formation of inclined sheets or circumferential intrusions is promoted (Grosfils, 2007; Gudmundsson, 1998). Rather than trapdoor faulting, we suggest that the pressurization of the sill-like hydrothermal system at Agung opened pathways to the fumarolic field located on the northeastern edge of the crater floor (Figures 3c and 3d). This resulted in increased flux through the fumarolic field (Figure 9a) (Andaru et al., 2021; Syahbana et al., 2019). Once fluid flow is present, erosion and dissolution can widen pathways without the need for surface displacement. Nevertheless, the opening of these pathways might still have produced displacement at the surface. Due to the steep slopes and unfortunate viewing geometries, we were not able to track persistent scatterers near or on the fumarolic field. However, one TSX ascending interferogram from 28 September to 20 October 2017 (Figure 4g), shows possible displacement fringes in the northeast corner of the crater floor that could be related to the opening of pathways to the fumarolic field.

We were not able to capture any co-eruptive displacements on the crater floor associated with the 21 November or subsequent eruptions. We can, however, discuss likely mechanisms for the explosion and the location of the

explosion crater. The November signal only shows 3–5 cm of LOS displacement but is likely capturing just the start of displacement leading up to the phreatomagmatic explosion as magma ascended to very shallow depths. The phreatomagmatic explosion on 21 November 2017, was probably a result of magma reaching the shallow hydrothermal system (Figure 9b), which flashed to steam and formed a vent in the center of the crater floor (Syahbana et al., 2019). We propose that the stresses imposed by this rapid volume change were orders of magnitude larger than those associated with the pressurization of the hydrothermal system, causing the vent to form in the center of the crater rather than in the fumarolic field. Then, on 25 November 2017, the magma ascended vertically and used the vent created by the phreatomagmatic explosion to reach the surface (Figure 9c). These observations highlight the different paths that can be taken by different fluids during phases of volcanic unrest and eruption.

6.3. Implications for Volcano Monitoring

We have shown that pre-eruptive intra-crater deformation at Agung is related to a shallow hydrothermal system at the summit. Many volcanic systems share similar characteristics to Agung: active stratovolcanoes with densely vegetated flanks and an exposed summit are present in several volcanic arcs in tropical environments, and shallow hydrothermal systems are found at several such volcanoes (e.g., La Soufrière (Guadeloupe) (Rosas-Carbajal et al., 2016), Kirishima (Japan) (Tajima et al., 2020; Tsukamoto et al., 2018), and El Chichón (Mexico) (Taran et al., 1998)). Here we discuss why the localized deformation has rarely been observed at other similar volcanoes.

The observation of localized deformation at volcanoes can be made difficult because of inhospitable or hard-to-reach terrain (e.g., steep slopes, high summits, deep crater floors), limiting the implementation of ground monitoring and increasing the reliance on satellites. The availability of high-resolution SAR satellite data through the CEOS Volcano Demonstrator Project (Pritchard et al., 2021), combined with an updated high-resolution DEM, allowed for the discovery of intra-crater deformation at Agung following the seismic unrest in September–October 2017. Using multiple SAR satellites and satellite tracks allowed for detailed analysis of the temporal evolution of the intra-crater deformation, including the serendipitous discovery of the November signal. If the November deformation signal had been detected before the eruption, it would have substantiated the presence of renewed unrest as indicated by the detection of anomalous CO₂ gas on the morning of the eruption. However, the (near) real-time analysis needed for crisis response requires frequent and regular acquisitions (currently only available for selected places) and dedicated automated processing.

We rely on the availability of accurate, high-resolution (<30 m) DEMs to detect and analyze strong and localized deformation signals, like those at Agung. The SRTM 90 m DEM, a standard choice for automated Sentinel-1 interferometry (e.g., LiCSAR Lazecký et al., 2020), is not suitable for measuring the shallow-sourced deformation signal at Agung or similar volcanoes (see Figure 5e). Accurate georeferencing is also important for interpretation of deformation signals (compare Figures 5c and 5d), and inaccurate georeferencing can cause data sets to be abandoned. The small footprint (350-by-400 m) of the deformation signal requires processing of satellite data at high-spatial-resolution to prevent under-sampling the deformation field. Over-sampling DEMs to roughly match the resolution of the SAR data can improve image quality (Small et al., 1998) (compare Figures 5a and 5f to 5b and 5g, respectively), but, when available, a high-resolution DEM is preferable. Accurate, high-resolution DEMs are, however, rarely open source and are therefore only available at limited locations or to selected researchers. Additionally, DEMs generated from optical satellite imagery (e.g., Bagnardi et al., 2016; Bernard et al., 2012) require cloud-free stereo images, limiting the potential in persistently cloud-covered areas like Indonesia (Mao et al., 2019). Open-data policies and UAV-based photogrammetry would allow for more frequent use of high-resolution DEMs.

Deep volcanic processes can affect the shallow parts of the volcanic system (e.g., hydrothermal system, conduit, flank instability) during the acceleration of unrest, resulting in localized deformation. It is, therefore, important to monitor for shallow-sourced localized deformation in order to perform more informed unrest detection and eruption forecasting. This event at Agung and those summarised in Table 1 show the need for frequent and regular analysis of surface displacement with high-resolution SAR data, especially where ground instrumentation is sparse. Improving the availability of high-resolution SAR data (e.g., from CSK, TSX, ICEYE, Capella Space (Stringham et al., 2019), or the prospective NISAR satellites) and accurate high-resolution DEMs for topographic correction (≤30 m resolution) will allow for improved monitoring of localized deformation. This study adds to the growing list of examples from the CEOS and Supersite Projects that show how monitoring with

high-resolution SAR data can lead to effective recognition of unrest and have helped to forecast hazardous activity (e.g., Merapi (Indonesia) (Pallister et al., 2013; Poland & Zebker, 2022), Latin America (Pritchard, Biggs, et al., 2018), Holuhraun (Sigmundsson et al., 2015), and Kilauea (Neal et al., 2019)), but data access remains a limitation in many cases.

7. Conclusions

The unrest prior to the 2017 eruption of Mount Agung provides a rare observation of intra-crater deformation at a stratovolcano. We were able to study this deformation in great detail using high-resolution Interferometric Synthetic Aperture Radar (InSAR) provided through the Committee on Earth Observing Satellites (CEOS) Volcano Demonstrator Project, which allowed us to link the pre-eruptive deformation to a shallow hydrothermal system. The deformation is best explained by a sill-like source less than 200 m below the crater floor. We achieved excellent temporal coverage by combining data from several SAR satellites, which made it possible to distinguish two stages of deformation. The first stage occurred together with the flank dyke intrusion and seismic activity northwest of the volcano and is probably the result of pressurization from the injection of magmatic gases. The second stage occurred within 4 days to 11 hr before the eruption started. The tight window for deformation, relative to the onset of eruption, points to the interaction of the hydrothermal system with ascending magma.

Crucial to the understanding of the shallow subsurface was the availability of high-resolution SAR data over the summit and an accurate high-resolution Digital Elevation Model (DEM). The deformation signal on the crater floor of Agung joins a short but growing list of localized volcano deformation detected with InSAR. Our ability to forecast volcanic activity and eruptions partly depends on the detection and understanding of these localized signals, especially in areas not covered by ground-based instruments. There is, therefore, a need for more high-resolution SAR data and increased data availability through projects like the CEOS Volcano Pilot and Demonstrator Projects to better facilitate the detection, monitoring, and interpretation of signals like that detected on the crater floor of Agung.

Data Availability Statement

The TSX/TDX and CSK SAR data were provided by the Deutsches Zentrum für Luft-und Raumfahrt (German Aerospace Center) and Agenzia Spaziale Italiana (Italian Space Agency), respectively, as part of the Centre for Earth Observing Satellites (CEOS) Volcano Demonstrator project and VDAP. The WorldView Level-1B images used for this study were made available under the NGA NextView license. The open-access Sentinel-1 data were obtained via the Alaska Satellite Foundation (ASF). SAR data were processed using GAMMA (version: December 2019) (Werner et al., 2000) (<https://www.gamma-rs.ch/software>) and open-source software StaMPS (version 4.1-beta) (Hooper et al., 2012) (<https://github.com/dbekaert/StaMPS/releases/tag/v4.1-beta>). Model inversion was performed using open-source GBIS (version 1.1) (Bagnardi & Hooper, 2018) (<https://comet.nerc.ac.uk/gbis/>). StaMPS time series output, GBIS model input, and solution files are available at Zenodo via <https://zenodo.org/record/7041377>. Data projection onto cross-sections was done using public-domain Generic Mapping Tools 6 (GMT6) (Wessel et al., 2013) (<https://www.generic-mapping-tools.org/>) and QGIS (version 3.20.3) (<https://www.qgis.org/en/site/>).

References

- AgustanKimata, F., Pamitro, Y. E., & Abidin, H. Z. (2012). Understanding the 2007–2008 eruption of Anak Krakatau Volcano by combining remote sensing technique and seismic data. *International Journal of Applied Earth Observation and Geoinformation*, 14(1), 73–82. <https://doi.org/10.1016/j.jag.2011.08.011>
- Akaike, H. (1974). A new look at the statistical model identification. *IEEE Transactions on Automatic Control*, 19(6), 716–723. <https://doi.org/10.1109/tac.1974.1100705>
- Albino, F., & Biggs, J. (2021). Magmatic processes in the east African rift system: Insights from a 2015–2020 sentinel-1 InSAR survey. *Geochemistry, Geophysics, Geosystems*, 22(3), e2020GC009488. <https://doi.org/10.1029/2020GC009488>
- Albino, F., Biggs, J., & Syahbana, D. K. (2019). Dyke intrusion between neighbouring arc volcanoes responsible for 2017 pre-eruptive seismic swarm at Agung. *Nature Communications*, 10(1), 1–11. <https://doi.org/10.1038/s41467-019-08564-9>
- Albino, F., Biggs, J., Yu, C., & Li, Z. (2020). Automated methods for detecting volcanic deformation using sentinel-1 InSAR time series illustrated by the 2017–2018 unrest at Agung, Indonesia. *Journal of Geophysical Research: Solid Earth*, 125(2), e2019JB017908. <https://doi.org/10.1029/2019JB017908>
- Albino, F., Pinel, V., Massol, H., & Collombet, M. (2011). Conditions for detection of ground deformation induced by conduit flow and evolution. *Journal of Geophysical Research*, 116(B6), B06201. <https://doi.org/10.1029/2010JB007871>

Acknowledgments

We thank Francisco Delgado, Jeremy Pesicek, and one anonymous reviewer for their thoughtful comments, which helped raise the quality of this work. We would also like to thank our colleagues at the USGS and CVGHM for their support and helpful discussion. We want to thank VDAP for providing the mosaic of the TSX and WV3 DEM over Agung. Any use of trade, firm, or product names is for descriptive purposes only and does not imply endorsement by the U.S. Government. MJWB, JB and SKE are members of the NERC Centre for the Observation and Modelling of Earthquakes, Volcanoes and Tectonics (COMET, <http://comet.nerc.ac.uk>), a partnership between UK Universities and the British Geological Survey. We want to thank COMET for their support and the use of their resources. MJWB is funded by the NERC GW4+ doctoral Training Partnership (S100413-110). For this project (JB) has received funding from the European Research Council (ERC) under the European Union's Horizon 2020 research and innovation programme (grant agreement 101003173), JB is also funded through the Leverhulme Prize (PLP-2018-362). SKE is funded by a NERC Independent Research Fellowship (NE/R015546/1).

- Alonso-González, A., Hajnsek, I., Grigorov, C., Roth, A., Marschalk, U., Martínez, N. G., et al. (2021). Joint PAZ and tandem-X missions interferometric performance. In *2021 IEEE International Geoscience and Remote Sensing Symposium IGARSS* (pp. 792–795). <https://doi.org/10.1109/IGARSS47720.2021.9554501>
- Amelung, F., Oppenheimer, C., Segall, P., & Zebker, H. (2000). Ground deformation near Gada 'Ale Volcano, Afar, observed by radar interferometry. *Geophysical Research Letters*, *27*(19), 3093–3096. <https://doi.org/10.1029/2000gl1008497>
- Andaru, R., Rau, J.-Y., Syahbana, D. K., Prayoga, A. S., & Purnamasari, H. D. (2021). The use of UAV remote sensing for observing lava dome emplacement and areas of potential lahar hazards: An example from the 2017–2019 eruption crisis at Mount Agung in Bali. *Journal of Volcanology and Geothermal Research*, *415*, 107255. <https://doi.org/10.1016/j.jvolgeores.2021.107255>
- Anderson, D., & Burnham, K. (2004). *Model selection and multi-model inference* (Vol. 63). Springer-Verlag
- Anderson, K. R., Poland, M. P., Johnson, J. H., & Miklius, A. (2015). Episodic deflation-inflation events at Kilauea Volcano and implications for the shallow magma system. *Hawaiian Volcanoes: From Source to Surface*, *208*, 229.
- Auker, M. R., Sparks, R. S. J., Siebert, L., Croweller, H. S., & Ewert, J. (2013). A statistical analysis of the global historical volcanic fatalities record. *Journal of Applied Volcanology*, *2*(1), 1–24. <https://doi.org/10.1186/2191-5040-2-2>
- Bagnardi, M., González, P. J., & Hooper, A. (2016). High-resolution digital elevation model from tri-stereo Pleiades-1 satellite imagery for lava flow volume estimates at Fogo Volcano. *Geophysical Research Letters*, *43*(12), 6267–6275. <https://doi.org/10.1002/2016gl069457>
- Bagnardi, M., & Hooper, A. (2018). Inversion of surface deformation data for rapid estimates of source parameters and uncertainties: A Bayesian Approach. *Geochemistry, Geophysics, Geosystems*, *19*(7), 2194–2211. <https://doi.org/10.1029/2018GC007585>
- Bekaert, D. P., Karim, M., Linick, J. P., Hua, H., Sangha, S., Lucas, M., & others (2019). Development of open-access standardized InSAR displacement products by the advanced rapid imaging and analysis (ARIA) project for natural hazards. In *Agu fall meeting abstracts* (Vol. G23A–04).
- Bemelmans, M. J., de van Zeeuw-Dalftsen, E., Poland, M. P., & Johanson, I. A. (2021). Insight into the May 2015 summit inflation event at Kilauea Volcano, Hawai'i. *Journal of Volcanology and Geothermal Research*, *415*, 107250. <https://doi.org/10.1016/j.jvolgeores.2021.107250>
- Benson, P. M., Heap, M. J., Lavallée, Y., Flaws, A., Hess, K.-U., Selvadurai, A., et al. (2012). Laboratory simulations of tensile fracture development in a volcanic conduit via cyclic magma pressurisation. *Earth and Planetary Science Letters*, *349*, 231–239. <https://doi.org/10.1016/j.epsl.2012.07.003>
- Bernard, M., Decluseau, D., Gabet, L., & Nonin, P. (2012). 3D capabilities of Pleiades satellite. *The International Archives of the Photogrammetry, Remote Sensing and Spatial Information Sciences*, *39*, B3–B557. <https://doi.org/10.5194/isprsarchives-xxxix-b3-553-2012>
- Beyer, R., Alexandrov, O., & McMichael, S. (2018). The Ames stereo pipeline: NASA's open source software for deriving and processing terrain data. *Earth and Space Science*, *5*(9), 537–548. <https://doi.org/10.1029/2018EA000409>
- Beyer, R., Alexandrov, O., & McMichael, S. (2019). *NeoGeographyToolkit/StereoPipeline: ASP 2.6.2*. Zenodo. <https://doi.org/10.5281/zenodo.3247734>
- Biggs, J., Anthony, E., & Ebinger, C. (2009). Multiple inflation and deflation events at Kenyan volcanoes, East African Rift. *Geology*, *37*(11), 979–982. <https://doi.org/10.1130/g30133a.1>
- Biggs, J., & Pritchard, M. (2017). Global volcano monitoring: What does it mean when volcanoes deform? *Elements*, *13*(1), 17–22. <https://doi.org/10.2113/gselements.13.1.17>
- Bonforte, A., & Puglisi, G. (2006). Dynamics of the eastern flank of Mt. Etna volcano (Italy) investigated by a dense GPS network. *Journal of Volcanology and Geothermal Research*, *153*(3), 357–369. <https://doi.org/10.1016/j.jvolgeores.2005.12.005>
- Cassidy, M., Ebmeier, S. K., Helo, C., Watt, S. F. L., Caudron, C., Odell, A., et al. (2019). Explosive eruptions with little warning: Experimental petrology and volcano monitoring observations from the 2014 eruption of Kelud, Indonesia. *Geochemistry, Geophysics, Geosystems*, *20*(8), 4218–4247. <https://doi.org/10.1029/2018GC008161>
- Castro, J. M., Cordonnier, B., Schipper, C. I., Tuffen, H., Baumann, T. S., & Feisel, Y. (2016). Rapid laccolith intrusion driven by explosive volcanic eruption. *Nature Communications*, *7*(1), 1–7. <https://doi.org/10.1038/ncomms13585>
- Casu, F., Manconi, A., Pepe, A., & Lanari, R. (2011). Deformation time-series generation in areas characterized by large displacement dynamics: The SAR amplitude pixel-offset SBAS technique. *IEEE Transactions on Geoscience and Remote Sensing*, *49*(7), 2752–2763. <https://doi.org/10.1109/TGRS.2010.2104325>
- Cayol, V., & Cornet, F. H. (1998). Effects of topography on the interpretation of the deformation field of prominent volcanoes—Application to Etna. *Geophysical Research Letters*, *25*(11), 1979–1982. <https://doi.org/10.1029/98GL51512>
- Chadwick, W. W., Jónsson, S., Geist, D. J., Poland, M., Johnson, D. J., Batt, S., et al. (2011). The May 2005 eruption of Fernandina volcano, Galápagos: The first circumferential dike intrusion observed by GPS and InSAR. *Bulletin of Volcanology*, *73*(6), 679–697. <https://doi.org/10.1007/s00445-010-0433-0>
- Chaussard, E., & Amelung, F. (2012). Precursory inflation of shallow magma reservoirs at west Sunda volcanoes detected by InSAR. *Geophysical Research Letters*, *39*(21). <https://doi.org/10.1029/2012gl053817>
- Delgado, F., Kubanek, J., Anderson, K., Lundgren, P., & Pritchard, M. (2019). Physicochemical models of effusive rhyolitic eruptions constrained with InSAR and DEM data: A case study of the 2011–2012 Cordón Caulle eruption. *Earth and Planetary Science Letters*, *524*, 115736. <https://doi.org/10.1016/j.epsl.2019.115736>
- De Oliveira, C. G., Paradella, W. R., & Da Silva, A. d. Q. (2011). Assessment of radargrammetric DSMs from TerraSAR-X stripmap images in a mountainous relief area of the Amazon region. *ISPRS Journal of Photogrammetry and Remote Sensing*, *66*(1), 67–72. <https://doi.org/10.1016/j.isprsjprs.2010.08.008>
- Dietterich, H. R., Poland, M. P., Schmidt, D. A., Cashman, K. V., Sherrod, D. R., & Espinosa, A. T. (2012). Tracking lava flow emplacement on the east rift zone of Kilauea, Hawai'i, with synthetic aperture radar coherence. *Geochemistry, Geophysics, Geosystems*, *13*(5), Q05001. <https://doi.org/10.1029/2011GC004016>
- Di Traglia, F., De Luca, C., Manzo, M., Nolesini, T., Casagli, N., Lanari, R., & Casu, F. (2021). Joint exploitation of space-borne and ground-based multitemporal InSAR measurements for volcano monitoring: The Stromboli volcano case study. *Remote Sensing of Environment*, *260*, 112441. <https://doi.org/10.1016/j.rse.2021.112441>
- Du, Y., Feng, G., Li, Z., Peng, X., Zhu, J., & Ren, Z. (2017). Effects of external digital elevation model inaccuracy on StaMPS-PS processing: A case study in Shenzhen, China. *Remote Sensing*, *9*(11), 1115. <https://doi.org/10.3390/rs9111115>
- Dualeh, E. W., Ebmeier, S. K., Wright, T. J., Albino, F., Naismith, A., Biggs, J., et al. (2021). Analyzing explosive volcanic deposits from satellite-based radar backscatter, Volcán de Fuego, 2018. *Journal of Geophysical Research: Solid Earth*, *126*(9), e2021JB022250. <https://doi.org/10.1029/2021JB022250>
- Dumont, Q., Cayol, V., Froger, J.-L., & Peltier, A. (2022). 22 years of satellite imagery reveal a major destabilization structure at Piton de la Fournaise. *Nature Communications*, *13*(1), 1–11. <https://doi.org/10.1038/s41467-022-30109-w>

- Dumont, S., Sigmundsson, F., Parks, M. M., Drouin, V. J., Pedersen, G. B., Jónsdóttir, I., et al. (2018). Integration of SAR data into monitoring of the 2014–2015 Holuhraun eruption, Iceland: Contribution of the Icelandic volcanoes supersite and the FutureVolc projects. *Frontiers of Earth Science*, 6, 231. <https://doi.org/10.3389/feart.2018.00231>
- Ebmeier, S. K., Andrews, B. J., Araya, M. C., Arnold, D. W. D., Biggs, J., Cooper, C., et al. (2018). Synthesis of global satellite observations of magmatic and volcanic deformation: Implications for volcano monitoring and the lateral extent of magmatic domains. *Journal of Applied Volcanology*, 7(1), 2. <https://doi.org/10.1186/s13617-018-0071-3>
- Ebmeier, S. K., Biggs, J., Mather, T., Elliott, J., Wadge, G., & Amelung, F. (2012). Measuring large topographic change with InSAR: Lava thicknesses, extrusion rate and subsidence rate at Santiaguito volcano, Guatemala. *Earth and Planetary Science Letters*, 335, 216–225. <https://doi.org/10.1016/j.epsl.2012.04.027>
- Ebmeier, S. K., Biggs, J., Mather, T. A., & Amelung, F. (2013). Applicability of InSAR to tropical volcanoes: Insights from Central America. *Geological Society, London, Special Publications*, 380(1), 15–37. <https://doi.org/10.1144/sp380.2>
- Ebmeier, S. K., Biggs, J., Muller, C., & Avard, G. (2014). Thin-skinned mass-wasting responsible for widespread deformation at Arenal volcano. *Frontiers of Earth Science*, 2, 35. <https://doi.org/10.3389/feart.2014.00035>
- Farr, T. G., Rosen, P. A., Caro, E., Crippen, R., Duren, R., Hensley, S., et al. (2007). The shuttle radar topography mission. *Reviews of Geophysics*, 45(2). <https://doi.org/10.1029/2005RG000183>
- Fialko, Y., Khazan, Y., & Simons, M. (2001). Deformation due to a pressurized horizontal circular crack in an elastic half-space, with applications to volcano geodesy. *Geophysical Journal International*, 146(1), 181–190. <https://doi.org/10.1046/j.1365-246x.2001.00452.x>
- Fontijn, K., Costa, F., Sutawidjaja, I., Newhall, C. G., & Herrin, J. S. (2015). A 5000-year record of multiple highly explosive mafic eruptions from Gunung Agung (Bali, Indonesia): Implications for eruption frequency and volcanic hazards. *Bulletin of Volcanology*, 77(7), 1–15. <https://doi.org/10.1007/s00445-015-0943-x>
- Geiger, H., Troll, V. R., Jolis, E. M., Deegan, F. M., Harris, C., Hilton, D. R., & Freda, C. (2018). Multi-level magma plumbing at Agung and Batur volcanoes increases risk of hazardous eruptions. *Scientific Reports*, 8(1), 1–14. <https://doi.org/10.1038/s41598-018-28125-2>
- González, P. J., Singh, K. D., & Tiampo, K. F. (2015). Shallow hydrothermal pressurization before the 2010 eruption of Mount Sinabung Volcano, Indonesia, observed by use of ALOS satellite radar interferometry. *Pure and Applied Geophysics*, 172(11), 3229–3245. <https://doi.org/10.1007/s00024-014-0915-7>
- Green, D. N., Neuberger, J., & Cayol, V. (2006). Shear stress along the conduit wall as a plausible source of tilt at Soufrière Hills volcano, Montserrat. *Geophysical Research Letters*, 33(10). <https://doi.org/10.1029/2006GL025890>
- Gregg, P., De Silva, S., & Grosfils, E. (2013). Thermomechanics of shallow magma chamber pressurization: Implications for the assessment of ground deformation data at active volcanoes. *Earth and Planetary Science Letters*, 384, 100–108. <https://doi.org/10.1016/j.epsl.2013.09.040>
- Grosfils, E. B. (2007). Magma reservoir failure on the terrestrial planets: Assessing the importance of gravitational loading in simple elastic models. *Journal of Volcanology and Geothermal Research*, 166(2), 47–75. <https://doi.org/10.1016/j.jvolgeores.2007.06.007>
- Gudmundsson, A. (1998). Magma chambers modeled as cavities explain the formation of rift zone central volcanoes and their eruption and intrusion statistics. *Journal of Geophysical Research*, 103(B4), 7401–7412. <https://doi.org/10.1029/97JB03747>
- Gudmundsson, A. (2006). How local stresses control magma-chamber ruptures, dyke injections, and eruptions in composite volcanoes. *Earth-Science Reviews*, 79(1–2), 1–31. <https://doi.org/10.1016/j.earscirev.2006.06.006>
- Gunawan, M. T., Kusnandar, R., Supendi, P., Nugraha, A. D., Puspito, N. T., Daryono, Z., et al. (2020). Analysis of swarm earthquakes around Mt. Agung Bali, Indonesia prior to November 2017 eruption using regional BMKG network. *Geoscience Letters*, 7(1), 14. <https://doi.org/10.1186/s40562-020-00163-7>
- Hamling, I. J., Williams, C. A., & Hreinsdóttir, S. (2016). Depressurization of a hydrothermal system following the August and November 2012 Te Maari eruptions of Tongariro, New Zealand. *Geophysical Research Letters*, 43(1), 168–175. <https://doi.org/10.1002/2015GL067264>
- Hanssen, R. F. (2001). *Radar interferometry: Data interpretation and error analysis* (Vol. 2). Springer Science and Business Media.
- Head, M., Hickey, J., Gottsmann, J., & Fournier, N. (2021). Exploring the impact of thermally controlled crustal viscosity on volcanic ground deformation. *Journal of Geophysical Research: Solid Earth*, 126(8), e2020JB020724. <https://doi.org/10.1029/2020JB020724>
- Hickey, J., & Gottsmann, J. (2014). Benchmarking and developing numerical Finite Element models of volcanic deformation. *Journal of Volcanology and Geothermal Research*, 280, 126–130. <https://doi.org/10.1016/j.jvolgeores.2014.05.011>
- Hickey, J., Gottsmann, J., Nakamichi, H., & Iguchi, M. (2016). Thermomechanical controls on magma supply and volcanic deformation: Application to Aira caldera. *Japan. Scientific reports*, 6(1), 1–10.
- Hickey, J., Lloyd, R., Biggs, J., Arnold, D., Mothes, P., & Muller, C. (2020). Rapid localized flank inflation and implications for potential slope instability at Tungurahua volcano, Ecuador. *Earth and Planetary Science Letters*, 534, 116104. <https://doi.org/10.1016/j.epsl.2020.116104>
- Holohan, E. P., Sudhaus, H., Walter, T. R., Schöpfer, M. P., & Walsh, J. J. (2017). Effects of host-rock fracturing on elastic-deformation source models of volcano deflation. *Scientific Reports*, 7(1), 1–12. <https://doi.org/10.1038/s41598-017-10009-6>
- Hooper, A. (2008). A multi-temporal InSAR method incorporating both persistent scatterer and small baseline approaches. *Geophysical Research Letters*, 35(16), L16302. <https://doi.org/10.1029/2008gl034654>
- Hooper, A., Bekaert, D., Spaans, K., & Arkan, M. (2012). Recent advances in SAR interferometry time series analysis for measuring crustal deformation. *Tectonophysics*, 514, 1–13. <https://doi.org/10.1016/j.tecto.2011.10.013>
- Hooper, A., Segall, P., & Zebker, H. (2007). Persistent scatterer interferometric synthetic aperture radar for crustal deformation analysis, with application to Volcán Alcedo, Galápagos. *Journal of Geophysical Research*, 112(B7), B07407. <https://doi.org/10.1029/2006jb004763>
- Hotta, K., Iguchi, M., Ohkura, K., & Yamamoto, T. (2016). Multiple-pressure-source model for ground inflation during the period of high explosivity at Sakurajima volcano, Japan—Combination analysis of continuous GNSS, tilt and strain data. *Journal of Volcanology and Geothermal Research*, 310, 12–25. <https://doi.org/10.1016/j.jvolgeores.2015.11.017>
- Hotta, K., Iguchi, M., & Tameguri, T. (2016). Rapid dike intrusion into Sakurajima volcano on August 15, 2015, as detected by multi-parameter ground deformation observations. *Earth Planets and Space*, 68(1), 1–9. <https://doi.org/10.1186/s40623-016-0450-0>
- Hutchison, W., Mather, T. A., Pyle, D. M., Biggs, J., & Yirgu, G. (2015). Structural controls on fluid pathways in an active rift system: A case study of the Aluto volcanic complex. *Geosphere*, 11(3), 542–562. <https://doi.org/10.1130/ges01119.1>
- Ignatenko, V., Laurila, P., Radius, A., Lamentowski, L., Antropov, O., & Muff, D. (2020). ICEYE Microsatellite SAR constellation status update: Evaluation of first commercial imaging modes. In *IGARSS 2020-2020 IEEE International Geoscience and Remote Sensing Symposium* (pp. 3581–3584). <https://doi.org/10.1109/IGARSS39084.2020.9324531>
- Italiana, A. S. (2007). *COSMO-SkyMed system description and user guide*. Rep. ASI-CSM-ENG-RS-093-A.
- Jackson, P., Shepherd, J. B., Robertson, R. E., & Skerritt, G. (1998). Ground deformation studies at Soufrière Hills Volcano, Montserrat I: Electronic distance meter studies. *Geophysical Research Letters*, 25(18), 3409–3412. <https://doi.org/10.1029/98gl01656>
- Johanson, I. A., & Bürgmann, R. (2005). Creep and quakes on the northern transition zone of the San Andreas fault from GPS and InSAR data. *Geophysical Research Letters*, 32(14). <https://doi.org/10.1029/2005GL023150>

- Jónsson, S. (2009). Stress interaction between magma accumulation and trapdoor faulting on Sierra Negra volcano, Galápagos. *Tectonophysics*, 471(1–2), 36–44. <https://doi.org/10.1016/j.tecto.2008.08.005>
- Jónsson, S., Zebker, H., & Amelung, F. (2005). On trapdoor faulting at Sierra Negra volcano, Galápagos. *Journal of Volcanology and Geothermal Research*, 144(1–4), 59–71. <https://doi.org/10.1016/j.jvolgeores.2004.11.029>
- Jónsson, S., Zebker, H., Segall, P., & Amelung, F. (2002). Fault slip distribution of the 1999 Mw 7.1 Hector mine, California, earthquake, estimated from satellite radar and GPS measurements. *Bulletin of the Seismological Society of America*, 92(4), 1377–1389. <https://doi.org/10.1785/0120000922>
- Kilbride, B. M., Edmonds, M., & Biggs, J. (2016). Observing eruptions of gas-rich compressible magmas from space. *Nature Communications*, 7(1), 1–8. <https://doi.org/10.1038/ncomms13744>
- Klees, R., & Massonnet, D. (1998). Deformation measurements using SAR interferometry: Potential and limitations. *Geologie en Mijnbouw*, 77(2), 161–176. <https://doi.org/10.1023/a:1003594502801>
- Kobayashi, T. (2018). Locally distributed ground deformation in an area of potential phreatic eruption, Midagahara volcano, Japan, detected by single-look-based InSAR time series analysis. *Journal of Volcanology and Geothermal Research*, 357, 213–223. <https://doi.org/10.1016/j.jvolgeores.2018.04.023>
- Kobayashi, T., Morishita, Y., & Munekane, H. (2018). First detection of precursory ground inflation of a small phreatic eruption by InSAR. *Earth and Planetary Science Letters*, 491, 244–254. <https://doi.org/10.1016/j.epsl.2018.03.041>
- Kusumadinata, K. (1964). *The eruption of the Batur volcano in Bali in 1963*. Volcanological Survey of Indonesia.
- Lamur, A., Kendrick, J., Eggertsson, G., Wall, R., Ashworth, J., & Lavallée, Y. (2017). The permeability of fractured rocks in pressurised volcanic and geothermal systems. *Scientific Reports*, 7(1), 1–9. <https://doi.org/10.1038/s41598-017-05460-4>
- Lazecký, M., Spaans, K., González, P. J., Maghsoudi, Y., Morishita, Y., Albino, F., et al. (2020). LiCSAR: An automatic InSAR tool for measuring and monitoring tectonic and volcanic activity. *Remote Sensing*, 12(15), 2430. <https://doi.org/10.3390/rs12152430>
- Lee, C.-W., Lu, Z., & Jung, H.-S. (2012). Simulation of time series surface deformation to validate a multi-interferogram InSAR processing technique. *International Journal of Remote Sensing*, 33(22), 7075–7087. <https://doi.org/10.1080/01431161.2012.700137>
- Li, S., Xu, W., & Li, Z. (2021). Review of the SBAS InSAR Time-series algorithms, applications, and challenges. *Geodesy and Geodynamics*, 13(2), 114–126. <https://doi.org/10.1016/j.geog.2021.09.007>
- Lohman, R. B., & Simons, M. (2005). Some thoughts on the use of InSAR data to constrain models of surface deformation: Noise structure and data downsampling. *Geochemistry, Geophysics, Geosystems*, 6(1). <https://doi.org/10.1029/2004GC000841>
- Lu, Z., & Dzurisin, D. (2014). InSAR imaging of Aleutian volcanoes. In *InSAR imaging of Aleutian volcanoes* (pp. 87–345). Springer.
- Mania, R., Walter, T. R., Belousova, M., Belousov, A., & Senyukov, S. L. (2019). Deformations and morphology changes associated with the 2016–2017 eruption sequence at Bezymianny volcano, Kamchatka. *Remote Sensing*, 11, 1278. <https://doi.org/10.3390/rs11111278>
- Manta, F., & Taisne, B. (2019). A Bayesian Approach to infer volcanic system parameters, timing, and size of Strombolian Events from a single tilt station. *Journal of Geophysical Research: Solid Earth*, 124(5), 5081–5100. <https://doi.org/10.1029/2018JB016882>
- Mao, K., Yuan, Z., Zuo, Z., Xu, T., Shen, X., & Gao, C. (2019). Changes in global cloud cover based on remote sensing data from 2003 to 2012. *Chinese Geographical Science*, 29(2), 306–315. <https://doi.org/10.1007/s11769-019-1030-6>
- Martini, F., Tassi, F., Vaselli, O., Del Petro, R., Martínez, M., del Laat, R. V., & Fernandez, E. (2010). Geophysical, geochemical and geodetic signals of reawakening at Turrialba volcano (Costa Rica) after almost 150 years of quiescence. *Journal of Volcanology and Geothermal Research*, 198(3), 416–432. <https://doi.org/10.1016/j.jvolgeores.2010.09.021>
- Massonnet, D., & Feigl, K. L. (1998). Radar interferometry and its application to changes in the Earth's surface. *Reviews of Geophysics*, 36(4), 441–500. <https://doi.org/10.1029/97RG03139>
- Masterlark, T. (2003). Finite element model predictions of static deformation from dislocation sources in a subduction zone: Sensitivities to homogeneous, isotropic, Poisson-solid, and half-space assumptions. *Journal of Geophysical Research*, 108(B11), 2540. <https://doi.org/10.1029/2002JB002296>
- McTigue, D. (1987). Elastic stress and deformation near a finite spherical magma body: Resolution of the point source paradox. *Journal of Geophysical Research*, 92(B12), 12931–12940. <https://doi.org/10.1029/jb092ib12p12931>
- Mittermayer, J., Wollstadt, S., Prats-Iraola, P., & Scheiber, R. (2014). The TerraSAR-X staring spotlight mode concept. *IEEE Transactions on Geoscience and Remote Sensing*, 52(6), 3695–3706. <https://doi.org/10.1109/TGRS.2013.2274821>
- Mogi, K. (1958). *Relations between the eruptions of various volcanoes and the deformations of the ground surfaces around them* (Vol. 36, pp 99–134). Earthquake Engineering Research Institute.
- Morishita, Y., Kobayashi, T., & Yarai, H. (2016). Three-dimensional deformation mapping of a dike intrusion event in Sakurajima in 2015 by exploiting the right- and left-looking ALOS-2 InSAR. *Geophysical Research Letters*, 43(9), 4197–4204. <https://doi.org/10.1002/2016GL068293>
- Muller, C., Biggs, J., Ebmeier, S. K., Mothes, P., Palacios, P. B., Jarrín, P., et al. (2018). Temporal evolution of the magmatic system at Tungurahua Volcano, Ecuador, detected by geodetic observations. *Journal of Volcanology and Geothermal Research*, 368, 63–72. <https://doi.org/10.1016/j.jvolgeores.2018.11.004>
- Narita, S., Ozawa, T., Aoki, Y., Shimada, M., Furuya, M., Takada, Y., & Murakami, M. (2020). Precursory ground deformation of the 2018 phreatic eruption on Iwo-Yama volcano, revealed by four-dimensional joint analysis of airborne and spaceborne InSAR. *Earth Planets and Space*, 72(1), 145. <https://doi.org/10.1186/s40623-020-01280-5>
- Neal, C. A., Brantley, S. R., Antolik, L., Babb, J. L., Burgess, M., Calles, K., et al. (2019). The 2018 rift eruption and summit collapse of Kilauea Volcano. *Science*, 363(6425), 367–374. <https://doi.org/10.1126/science.aav7046>
- Odbert, H. M., Ryan, G. A., Mattioli, G. S., Hautmann, S., Gottsmann, J., Fournier, N., & Herd, R. A. (2014). Chapter 11 volcano geodesy at the Soufrière Hills Volcano, Montserrat: A review. *Geological Society, London, Memoirs*, 39(1), 195–217. <https://doi.org/10.1144/M39.11>
- Okada, Y. (1992). Internal deformation due to shear and tensile faults in a half-space. *Bulletin of the Seismological Society of America*, 82(2), 1018–1040. <https://doi.org/10.1785/bssa0820021018>
- Ozawa, T., & Ueda, H. (2011). Advanced interferometric synthetic aperture radar (InSAR) time series analysis using interferograms of multiple-orbit tracks: A case study on Miyake-jima. *Journal of Geophysical Research*, 116(B12), B12407. <https://doi.org/10.1029/2011JB008489>
- Pagli, C., Wright, T. J., Ebinger, C. J., Yun, S.-H., Cann, J. R., Barnie, T., & Ayele, A. (2012). Shallow axial magma chamber at the slow-spreading Ertá Ale Ridge. *Nature Geoscience*, 5(4), 284–288. <https://doi.org/10.1038/ngeo1414>
- Pallister, J. S., Schneider, D. J., Griswold, J. P., Keeler, R. H., Burton, W. C., Noyles, C., et al. (2013). Merapi 2010 eruption—Chronology and extrusion rates monitored with satellite radar and used in eruption forecasting. *Journal of Volcanology and Geothermal Research*, 261, 144–152. <https://doi.org/10.1016/j.jvolgeores.2012.07.012>
- Parker, A. L., Biggs, J., Walters, R. J., Ebmeier, S. K., Wright, T. J., Teanby, N. A., & Lu, Z. (2015). Systematic assessment of atmospheric uncertainties for InSAR data at volcanic arcs using large-scale atmospheric models: Application to the Cascade volcanoes, United States. *Remote Sensing of Environment*, 170, 102–114. <https://doi.org/10.1016/j.rse.2015.09.003>

- Pavez, A., Remy, D., Bonvalot, S., Diament, M., Gabalda, G., Froger, J.-L., et al. (2006). Insight into ground deformations at Lascar volcano (Chile) from SAR interferometry, photogrammetry and GPS data: Implications on volcano dynamics and future space monitoring. *Remote Sensing of Environment*, 100(3), 307–320. <https://doi.org/10.1016/j.rse.2005.10.013>
- Pinel, V., Hooper, A., De la Cruz-Reyna, S., Reyes-Davila, G., Doin, M. P., & Bascou, P. (2011). The challenging retrieval of the displacement field from InSAR data for andesitic stratovolcanoes: Case study of Popocatepetl and Colima Volcano, Mexico. *Journal of Volcanology and Geothermal Research*, 200(1–2), 49–61. <https://doi.org/10.1016/j.jvolgeores.2010.12.002>
- Pinel, V., Poland, M., & Hooper, A. (2014). Volcanology: Lessons learned from synthetic aperture radar imagery. *Journal of Volcanology and Geothermal Research*, 289, 81–113. <https://doi.org/10.1016/j.jvolgeores.2014.10.010>
- Poland, M. P. (2014). Time-averaged discharge rate of subaerial lava at Kilauea Volcano, Hawai'i, measured from TanDEM-X interferometry: Implications for magma supply and storage during 2011–2013. *Journal of Geophysical Research: Solid Earth*, 119(7), 5464–5481. <https://doi.org/10.1002/2014JB011132>
- Poland, M. P., & de Zeeuw-van Dalssen, E. (2021). Volcano geodesy: A critical tool for assessing the state of volcanoes and their potential for hazardous eruptive activity. In *Forecasting and planning for volcanic hazards, risks, and disasters* (pp. 75–115). Elsevier.
- Poland, M. P., Lopez, T., Wright, R., & Pavolonis, M. J. (2020). Forecasting, detecting, and tracking volcanic eruptions from space. *Remote Sensing in Earth Systems Sciences*, 3(1), 55–94. <https://doi.org/10.1007/s41976-020-00034-x>
- Poland, M. P., Takahashi, T. J., & Landowski, C. M. (2014). *Characteristics of Hawaiian volcanoes*. Government Printing Office.
- Poland, M. P., & Zebker, H. A. (2022). Volcano geodesy using InSAR in 2020: The past and next decades. *Bulletin of Volcanology*, 84(3), 1–8. <https://doi.org/10.1007/s00445-022-01531-1>
- Pritchard, M., Biggs, J., Wauthier, C., Sansosti, E., Arnold, D. W. D., Delgado, F., et al. (2018). Towards coordinated regional multi-satellite InSAR volcano observations: Results from the Latin America pilot project. *Journal of Applied Volcanology*, 7(1), 5. <https://doi.org/10.1186/s13617-018-0074-0>
- Pritchard, M., de Silva, S. L., Michelfelder, G., Zandt, G., McNutt, S. R., Gottsmann, J., et al. (2018). Synthesis: PLUTONS: Investigating the relationship between pluton growth and volcanism in the central Andes. *Geosphere*, 14(3), 954–982. <https://doi.org/10.1130/GES01578.1>
- Pritchard, M., Ebmeier, S., Poland, M., Biggs, J., Hamling, I., Aoki, Y., et al. (2021). Contrasting volcanic activity across Latin America, South-east Asia, and Africa with multi-parameter satellite monitoring data: The CEOS volcano demonstrator. *AGU fall meeting abstracts*, 2021, G24B–G03.
- Pritchard, M., Simons, M., Rosen, P., Hensley, S., & Webb, F. (2002). Co-seismic slip from the 1995 July 30 Mw = 8.1 Antofagasta, Chile, earthquake as constrained by InSAR and GPS observations. *Geophysical Journal International*, 150(2), 362–376. <https://doi.org/10.1046/j.1365-246x.2002.01661.x>
- Pritchard, M., & Yun, S.-H. (2018). In R. Singh & D. Bartlett (Eds.), *Satellite radar imaging and its application to natural hazards*. *Natural Hazards* (pp. 95–114).
- Purcell, V., Reddin, E., Ebmeier, S., González, P. J., Watson, A., Morishita, Y., & Elliott, J. (2022). Nearly three centuries of lava flow subsidence at Timanfaya, Lanzarote. *Geochemistry, Geophysics, Geosystems*, 23(10), e2022GC010576. <https://doi.org/10.1029/2022GC010576>
- Raggam, H., Gutjahr, K., Perko, R., & Schardt, M. (2010). Assessment of the stereo-radargrammetric mapping potential of TerraSAR-X Multi-beam spotlight data. *IEEE Transactions on Geoscience and Remote Sensing*, 48(2), 971–977. <https://doi.org/10.1109/TGRS.2009.2037315>
- Richter, N., Poland, M. P., & Lundgren, P. R. (2013). TerraSAR-X interferometry reveals small-scale deformation associated with the summit eruption of Kilauea Volcano, Hawai'i. *Geophysical Research Letters*, 40(7), 1279–1283. <https://doi.org/10.1002/grl.50286>
- Richter, N., Salzer, J. T., devan Zeeuw-Dalssen, E., Perissin, D., & Walter, T. R. (2018). Constraints on the geomorphological evolution of the nested summit craters of Lascar volcano from high spatio-temporal resolution TerraSAR-X interferometry. *Bulletin of Volcanology*, 80(3), 1–17.
- Rodríguez, E., Morris, C. S., & Belz, J. E. (2006). A global assessment of the SRTM performance. *Photogrammetric Engineering and Remote Sensing*, 72(3), 249–260. <https://doi.org/10.14358/pers.72.3.249>
- Rosas-Carbajal, M., Komorowski, J.-C., Nicollin, F., & Gibert, D. (2016). Volcano electrical tomography unveils edifice collapse hazard linked to hydrothermal system structure and dynamics. *Scientific Reports*, 6(1), 1–11. <https://doi.org/10.1038/srep29899>
- Ruch, J., Manconi, A., Zeni, G., Solaro, G., Pepe, A., Shirzaei, M., et al. (2009). Stress transfer in the Lazufre volcanic area, central Andes. *Geophysical Research Letters*, 36(22), L22303. <https://doi.org/10.1029/2009GL041276>
- Sahara, D. P., Rahsetyo, P. P., Nugraha, A. D., Syahbana, D. K., Widiyantoro, S., Zulfakriza, Z., et al. (2021). Use of local seismic network in analysis of volcano-tectonic (VT) events preceding the 2017 Agung volcano eruption (Bali, Indonesia). *Frontiers of Earth Science*, 9, 342. <https://doi.org/10.3389/feart.2021.619801>
- Salzer, J. T., Nikkhoo, M., Walter, T. R., Sudhaus, H., Reyes-Dávila, G., Bretón, M., & Arámbula, R. (2014). Satellite radar data reveal short-term pre-explosive displacements and a complex conduit system at Volcán de Colima, Mexico. *Frontiers of Earth Science*, 2(June), 1–11. <https://doi.org/10.3389/feart.2014.00012>
- Schaefer, L. N., Di Traglia, F., Chaussard, E., Lu, Z., Nolesini, T., & Casagli, N. (2019). Monitoring volcano slope instability with synthetic aperture radar: A review and new data from Pacaya (Guatemala) and Stromboli (Italy) volcanoes. *Earth-Science Reviews*, 192, 236–257. <https://doi.org/10.1016/j.earscirev.2019.03.009>
- Schaefer, L. N., Wang, T., Escobar-Wolf, R., Oommen, T., Lu, Z., Kim, J., et al. (2017). Three-dimensional displacements of a large volcano flank movement during the May 2010 eruptions at Pacaya Volcano, Guatemala. *Geophysical Research Letters*, 44(1), 135–142. <https://doi.org/10.1002/2016GL071402>
- Self, S., & King, A. J. (1996). Petrology and sulfur and chlorine emissions of the 1963 eruption of Gunung Agung, Bali, Indonesia. *Bulletin of Volcanology*, 58(4), 263–285. <https://doi.org/10.1007/s004450050139>
- Self, S., & Rampino, M. R. (2012). The 1963–1964 eruption of Agung volcano (Bali, Indonesia). *Bulletin of Volcanology*, 74(6), 1521–1536. <https://doi.org/10.1007/s00445-012-0615-z>
- Sennert, S. K. E. (2020). *Report on Agung (Indonesia)*. Smithsonian Institution and US Geological Survey.
- Shean, D. E., Alexandrov, O., Moratto, Z. M., Smith, B. E., Joughin, I. R., Porter, C., & Morin, P. (2016). An automated, open-source pipeline for mass production of digital elevation models (DEMs) from very-high-resolution commercial stereo satellite imagery. *ISPRS Journal of Photogrammetry and Remote Sensing*, 116, 101–117. <https://doi.org/10.1016/j.isprsjprs.2016.03.012>
- Shreve, T., Grandin, R., Boichu, M., Garaebiti, E., Moussallam, Y., Ballu, V., et al. (2019). From prodigious volcanic degassing to caldera subsidence and quiescence at Ambrym (Vanuatu): The influence of regional tectonics. *Scientific Reports*, 9(1), 1–13. <https://doi.org/10.1038/s41598-019-55141-7>
- Sigmundsson, F., Hooper, A., Hreinsdóttir, S., Vogfjörð, K. S., Ófeigsson, B. G., Heimisson, E. R., et al. (2015). Segmented lateral dyke growth in a rifting event at Bárðarbunga volcanic system, Iceland. *Nature*, 517(7533), 191–195. <https://doi.org/10.1038/nature14111>

- Small, D., Holecz, F., Meier, E., & Nüesch, D. (1998). Radiometric normalization for multimode image comparison. *Proceedings of the European Conference on Synthetic Aperture Radar*, (Vol. 98, pp. 25–27).
- Stephens, K., Ebmeier, S., Young, N., & Biggs, J. (2017). Transient deformation associated with explosive eruption measured at Masaya volcano (Nicaragua) using Interferometric Synthetic Aperture Radar. *Journal of Volcanology and Geothermal Research*, *344*, 212–223. <https://doi.org/10.1016/j.jvolgeores.2017.05.014>
- Stringham, C., Farquharson, G., Castelletti, D., Quist, E., Riggi, L., Eddy, D., & Soenen, S. (2019). The capella X-band SAR constellation for rapid imaging. In *IGARSS 2019-2019 IEEE International Geoscience and Remote Sensing Symposium* (pp. 9248–9251).
- Syahbana, D. K., Kasbani, K., Suantika, G., Prambada, O., Andreas, A. S., Saing, U. B., et al. (2019). The 2017–19 activity at Mount Agung in Bali (Indonesia): Intense unrest, monitoring, crisis response, evacuation, and eruption. *Scientific Reports*, *9*(1), 1–17. <https://doi.org/10.1038/s41598-019-45295-9>
- Symonds, R. B., Gerlach, T. M., & Reed, M. H. (2001). Magmatic gas scrubbing: Implications for volcano monitoring. *Journal of Volcanology and Geothermal Research*, *108*(1–4), 303–341. [https://doi.org/10.1016/S0377-0273\(00\)00292-4](https://doi.org/10.1016/S0377-0273(00)00292-4)
- Tajima, Y., Nakada, S., Maeno, F., Huruzono, T., Takahashi, M., Inamura, A., et al. (2020). Shallow magmatic hydrothermal eruption in April 2018 on Ebinokogen Ioyama volcano in Kirishima volcano group, Kyushu, Japan. *Geosciences*, *10*(5), 1–25. <https://doi.org/10.3390/geosciences10050183>
- Tanguy, J.-C., Ribière, C., Scarth, A., & Tjetjep, W. (1998). Victims from volcanic eruptions: A revised database. *Bulletin of Volcanology*, *60*(2), 137–144. <https://doi.org/10.1007/s004450050222>
- Taran, Y., Fischer, T. P., Pokrovsky, B., Sano, Y., Armienta, M. A., & Macias, J. L. (1998). Geochemistry of the volcano-hydrothermal system of El Chichón volcano, Chiapas, Mexico. *Bulletin of Volcanology*, *59*(6), 436–449. <https://doi.org/10.1007/s004450050202>
- Teunissen, P. J. (2006). *Testing theory*. VSSD Delft.
- Thollard, F., Clesse, D., Doin, M.-P., Donadieu, J., Durand, P., Grandin, R., et al. (2021). Flatsim: The form@ter large-scale multi-temporal sentinel-1 interferometry service. *Remote Sensing*, *13*(18), 3734. <https://doi.org/10.3390/rs13183734>
- Tobita, M., Murakami, M., Nakagawa, H., Yurai, H., Fujiwara, S., & Rosen, P. A. (2001). 3-D surface deformation of the 2000 Usu eruption measured by matching of SAR images. *Geophysical Research Letters*, *28*(22), 4291–4294. <https://doi.org/10.1029/2001gl013329>
- Toodesh, R., Verhagen, S., & Dagla, A. (2021). Prediction of changes in seafloor depths based on time series of bathymetry observations: Dutch North Sea case. *Journal of Marine Science and Engineering*, *9*(9), 931. <https://doi.org/10.3390/jmse9090931>
- Tsukamoto, K., Aizawa, K., Chiba, K., Kanda, W., Uyeshima, M., Koyama, T., et al. (2018). Three-dimensional resistivity structure of Iwo-Yama volcano, Kirishima volcanic complex, Japan: Relationship to shallow seismicity, surface uplift, and a small phreatic eruption. *Geophysical Research Letters*, *45*(23), 12821–12828. <https://doi.org/10.1029/2018GL080202>
- Voight, B., Hoblitt, R., Clarke, A., Lockhart, A., Miller, A., Lynch, L., & McMahon, J. (1998). Remarkable cyclic ground deformation monitored in real-time on Montserrat, and its use in eruption forecasting. *Geophysical Research Letters*, *25*(18), 3405–3408. <https://doi.org/10.1029/98gl01160>
- Wadge, G., Mattioli, G., & Herd, R. (2006). Ground deformation at Soufrière Hills Volcano, Montserrat during 1998–2000 measured by radar interferometry and GPS. *Journal of Volcanology and Geothermal Research*, *152*(1–2), 157–173. <https://doi.org/10.1016/j.jvolgeores.2005.11.007>
- Walter, T. R., Haghshenas Haghighi, M., Schneider, F. M., Coppola, D., Motagh, M., Saul, J., et al. (2019). Complex hazard cascade culminating in the Anak Krakatau sector collapse. *Nature Communications*, *10*(1), 4339. <https://doi.org/10.1038/s41467-019-12284-5>
- Wang, X., & Aoki, Y. (2019). Post-eruptive thermoelastic deflation of intruded magma in Usu volcano, Japan, 1992–2017. *Journal of Geophysical Research: Solid Earth*, *124*(1), 335–357. <https://doi.org/10.1029/2018JB016729>
- Wang, X., Aoki, Y., & Chen, J. (2019). Surface deformation of Asama volcano, Japan, detected by time series InSAR combining persistent and distributed scatterers, 2014–2018. *Earth Planets and Space*, *71*(1), 1–16. <https://doi.org/10.1186/s40623-019-1104-9>
- Wellik, J. J., Prejean, S. G., & Syahbana, D. K. (2021). Repeating earthquakes during multiple phases of unrest and eruption at Mount Agung, Bali, Indonesia, 2017. *Frontiers of Earth Science*, *9*, 369. <https://doi.org/10.3389/feart.2021.653164>
- Werner, C., Wegmüller, U., Strozzi, T., & Wiesmann, A. (2000). *GAMMA SAR and interferometric processing software* (pp. 211–219). European Space Agency, (Special Publication) ESA SP.
- Wessel, P., Smith, W. H. F., Scharroo, R., Luis, J., & Wobbe, F. (2013). Generic mapping tools: Improved version released. *Eos, Transactions American Geophysical Union*, *94*(45), 409–410. <https://doi.org/10.1002/2013EO450001>
- Williams, C. A., & Wadge, G. (1998). The effects of topography on magma chamber deformation models: Application to Mt. Etna and radar interferometry. *Geophysical Research Letters*, *25*(10), 1549–1552. <https://doi.org/10.1029/98gl01136>
- Wong, Y.-Q., & Segall, P. (2020). Joint inversions of ground deformation, extrusion flux, and gas emissions using physics-based models for the mount st. Helens 2004–2008 eruption. *Geochemistry, Geophysics, Geosystems*, *21*(12), e2020GC009343. <https://doi.org/10.1029/2020GC009343>
- Yang, X.-M., Davis, P. M., & Dieterich, J. H. (1988). Deformation from inflation of a dipping finite prolate spheroid in an elastic half-space as a model for volcanic stressing. *Journal of Geophysical Research*, *93*(B5), 4249–4257. <https://doi.org/10.1029/jb093ib05p04249>
- Yip, S. T. H., Biggs, J., & Albino, F. (2019). Reevaluating volcanic deformation using atmospheric corrections: Implications for the magmatic system of Agung volcano, Indonesia. *Geophysical Research Letters*, *46*(23), 13704–13711. <https://doi.org/10.1029/2019gl085233>
- Yip, S. T. H., Biggs, J., Edmonds, M., Liggins, P., & Shorttle, O. (2022). Contrasting volcanic deformation in arc and ocean island settings due to exsolution of magmatic water. *Geochemistry, Geophysics, Geosystems*, *23*(7), e2022GC010387. <https://doi.org/10.1029/2022GC010387>
- Yu, H., Lan, Y., Yuan, Z., Xu, J., & Lee, H. (2019). Phase unwrapping in InSAR: A review. *IEEE Geoscience and Remote Sensing Magazine*, *7*(1), 40–58. <https://doi.org/10.1109/mgrs.2018.2873644>
- Yun, S.-H., Segall, P., & Zebker, H. (2006). Constraints on magma chamber geometry at Sierra Negra volcano, Galápagos islands, based on InSAR observations. *Journal of Volcanology and Geothermal Research*, *150*(1), 232–243. <https://doi.org/10.1016/j.jvolgeores.2005.07.009>
- Yun, S.-H., Zebker, H., Segall, P., Hooper, A., & Poland, M. (2007). Interferogram formation in the presence of complex and large deformation. *Geophysical Research Letters*, *34*(12), L12305. <https://doi.org/10.1029/2007GL029745>
- Yunjun, Z., Amelung, F., & Aoki, Y. (2021). Imaging the hydrothermal system of Kirishima volcanic complex, Japan with L-band InSAR time series. *Geophysical Research Letters*, *48*(11), 1–12. <https://doi.org/10.1029/2021gl092879>
- Zebker, H. A., Rosen, P., Hensley, S., & Mouginiis-Mark, P. J. (1996). Analysis of active lava flows on Kīlauea volcano, Hawai‘i, using SIR-C radar correlation measurements. *Geology*, *24*(6), 495–498. [https://doi.org/10.1130/0091-7613\(1996\)024<0495:AOALFO>2.3.CO;2](https://doi.org/10.1130/0091-7613(1996)024<0495:AOALFO>2.3.CO;2)
- Zen, M., & Hadikusumo, D. (1964). Preliminary report on the 1963 eruption of Mt. Agung in Bali (Indonesia). *Bulletin Volcanologique*, *27*(1), 269–299. <https://doi.org/10.1007/bf02597526>

References From the Supporting Information

- Gelman, A., Gilks, W. R., & Roberts, G. O. (1997). Weak convergence and optimal scaling of random walk metropolis algorithms. *Annals of Applied Probability*, 7(1), 110–120. <https://doi.org/10.1214/aop/1034625254>